Ideal MHD Instabilities as an Initial Boundary-Value Problem

G. Bateman, W. Schneider, W. Grossmann

IPP 1/145 April 1974

MAX-PLANCK-INSTITUT FÜR PLASMAPHYSIK

GARCHING BEI MÜNCHEN

MAX-PLANCK-INSTITUT FÜR PLASMAPHYSIK

GARCHING BEI MÜNCHEN

Ideal MHD Instabilities as an Initial Boundary-Value Problem

G. Bateman, W. Schneider, W. Grossmann

IPP 1/145 April 1974

Die nachstehende Arbeit wurde im Rahmen des Vertrages zwischen dem Max-Planck-Institut für Plasmaphysik und der Europäischen Atomgemeinschaft über die Zusammenarbeit auf dem Gebiete der Plasmaphysik durchgeführt.

IPP 1/145 G.Bateman+
W.Schneider
W.Grossmann‡

Ideal MHD Instabilities as an Initial Boundary-Value Problem

April 1974 (in English)

Abstract

The gross MHD instabilities of straight cylindrical plasmas with elongated cross-section are investigated by solving the linearized MHD equations as an initial boundary-value problem on the computer. The linearized equations are Fourier analyzed along the ignorable coordinate of the equilibrium in order to reduce the computation to two dimensions. The method is applied to find the fixed-boundary instabilities of an equilibrium with rectangular walls. Starting with an arbitrary initial perturbation and following it for many Alfven transit times, we find that the dominant instability overwhelms all stable oscillations after several e-folding times. We determine the growth rates of the fastest growing instabilities as a function of the equilibrium parameters. Then we examine the spatial structure of the physical variables ($\underline{v}^1, \underline{B}^1, p^1$). We find that the cross section of the velocity field displays a distinctive convection pattern. This structure becomes spatially concentrated around the point of maximum rotational transform as the equilibrium current is decreased to the marginal point and concentrates near the wall as the current is increased. Given the equilibrium $p'(\psi) = J_{zc}\psi/\psi_c$, $\psi(\text{wall}) = 0$, we find that the marginal current density J_{zc} for each mode increases as the cross section is elongated. But the growth rates of the higher azimuthal m-modes increase with elongation and their intervals of instability overlap with the lower m-modes.

I N D E X

1. Introduction

By elongating the cross section of Tokamaks and Pinches it is hoped that higher current densities may be used for stable plasma confinement /1/, /2/, /3/. Raising the current density should increase the plasma beta β ($\beta = p/(p+B^2/2)$) and should improve Ohmic heating. Computer methods are available for calculating these two-dimensional MHD equilibria given the profiles ($p(\psi)$ and $rB_\varphi = I(\psi)$), boundary conditions and central current density J_{tc} /4/, /5/, /6/. However, the current density of these devices is thought to be limited not by equilibrium considerations but by the effect of gross MHD instabilities. What is needed then is a method for studying the instabilities of any computed two-dimensional equilibrium. We have developed a computer code for this purpose. One of the immediate goals of this study is to determine what equilibrium shape and profile is needed to achieve the highest possible current density (or β) within the plasma. A longer range goal is to understand the nature of the driving forces and the ultimate physical effects of gross MHD instabilities when they exist.

One of the simplest and most flexible ways to study instabilities with a computer is to integrate the MHD equations forward in time starting with an arbitrary initial perturbation -- or, more precisely, to solve the initial boundary-value problem. By linearizing the MHD equations and considering one Fourier component (in the ignorable direction of the equilibrium) at a time, we reduce the computation to two dimensions. For an unstable equilibrium, the fastest exponentially-growing mode ultimately dominates over all other motion making it a simple matter to determine the growth rate and the spatial form of the instability eigenfunction. The results are independent of the initial conditions provided the initial perturbation is not completely orthogonal to the fastest growing eigenfunction. No expansions or approximations are used -- although practical considerations limit the method to high-β equilibria with smooth current profiles and to gross instabilities.

The most important limitation of the model in its present form is that the ideal MHD equations are applied throughout the domain -- there is no vacuum or resistive region outside the plasma (although the equilibrium current and pressure may be zero around a central part of the domain). Hence the instabilities studied here must be classified as "fixed-boundary modes" /7/ or "internal kink modes" /8/ as opposed to "free-boundary kink" instabilities where the singular surface lies in a vacuum region and the flux surfaces there are able to change topology. This change in topology may be a crucial effect making the

physical consequences of the modes entirely different. However, estimates made for the circular cylinder equilibrium imply that the growth rates of the modes may be comparable under the conditions of high-β and low aspect ratio considered here /7/, /9/.

The practical restriction to high-β comes from the observation that the growth rate scales with the B-field induced by the plasma currents while the rate of computed plasma motion scales with the total B-field. The lower the β, the slower the growth rate compared to the computation rate. More precisely, the computation rate is determined by the maximum magnetosonic velocity $v_{MS} = (B^2/\rho + \gamma p/\rho)^{1/2}$ over the domain. Therefore we must avoid zero density ρ, and the incompressible limit $\gamma \longrightarrow \infty$, and low β, $p << B^2$.

This work on the linear equations may be considered as the first step to a full study of the gross plasma instabilities. The experience and results gained here are a useful starting point for the nonlinear three-dimensional problem, as well as for various non-ideal MHD models which include, for example, resistivity (as an approximation to the free-boundary kink instability problem), viscosity, and other transport effects.

In section 2 we describe the model in its analytic form. The essential points of the numerical procedure are presented in section 3. Section 4 begins with a qualitative discussion of the instabilities before presenting graphical summaries of the growth rates and marginal points which were found for a particular equilibrium.

2. MHD-Model

2.1 Basic Equations

The ideal MHD equations provide one of the simplest models for describing the gross motion of a plasma /10/. They may be thought of as a simplified form of the moment equations without transport coefficients, and Maxwell's equations. The continuity equation (1) prescribes the time- and space-dependence of the mass density ϱ; the evolution of the fluid velocity $\vec{v}$ is determined by the equation of motion (2) and the plasma pressure p by the pressure equation (3). Faraday's law (4) describes the development of the magnetic field $\vec{B}$; Ampere's law (5) determines the current density J and Ohm's law (6) the electric field $\vec{E}$.

$$\frac{\partial}{\partial t}\varrho + \nabla\cdot(\varrho\vec{v}) = 0 \qquad (1)$$

$$\varrho\left(\frac{\partial}{\partial t} + \vec{v}\cdot\nabla\right)\vec{v} + \nabla p - \vec{J}\times\vec{B} = 0 \qquad (2)$$

$$\frac{\partial}{\partial t} p + \nabla\cdot(p\vec{v}) + (\gamma-1)\, p\,(\nabla\cdot\vec{v}) = 0 \qquad (3)$$

$$\frac{\partial}{\partial t}\vec{B} + \nabla\times\vec{E} = 0 \qquad (4)$$

$$\vec{J} = \nabla\times\vec{B} \qquad (5)$$

$$\vec{E} + \vec{v}\times\vec{B} = 0 \qquad (6)$$

The condition $\nabla\cdot\vec{B} = 0$ is preserved by Faraday's law if it is imposed initially. The charge density $\sigma = \nabla\cdot\vec{E}$ is not calculated, since it is not needed in any of the equations. The combination of the equation of continuity and the pressure equation yield the adiabatic equation of state (conservation of entropy):

$$\left(\frac{\partial}{\partial t} + \vec{v}\cdot\nabla\right)\left(p\varrho^{-\gamma}\right) = 0$$

By means of this relation the mass density could be eliminated.

The equations are written here in rationalized Gaussian units with c= 1 (c...speed of light). Dimensionless forms will be provided later (4.2) to facilitate conversion to other units.

2.2 Linearization and Fourier Transformation

We shall now discuss our reasons for choosing to consider the linearized form of the above equations and for taking the Fourier transform of the perturbed quantities along the ignorable coordinate of the equilibrium.

The most fundamental reason for linearizing the equations is that the results may then be expressed as the sum of eigenfunctions. The advantage is that the form of each eigenfunction depends upon only the form of the equilibrium and is independent of the choice of initial perturbation. Also a good deal is known about the properties of the eigenfunctions. The eigenfunction decomposition of each of the perturbation variables may be written

$$U(x,t) = U_{\gamma_1}(x)\, e^{\gamma_1 t} + U_{\gamma_2}(x)\, e^{\gamma_2 t} + \ldots + \int d\omega\, U_{\omega}(x)\, e^{i\omega t}$$

It can be proved in general that all the eigenvalues γ_1, γ_2 ,... and ω are real -- there is no overstablitiy /10/. Under some conditions algebraic growth can arise from the real spectrum in the neighbourhood of $\omega = 0$ and exponentially damped oscillations can be extracted from the continous spectrum in much the same manner as Landau damping can arise from the continous Case-Van Kampen spectrum of the Vlasov equation /11/. When solving the initial value problem with an arbitrary initial perturbation, we first observe MHD oscillations whose period is given by the average magnetosonic velocity transit time. If an unstable plasma is allowed to evolve long enough, the fastest growing mode ultimately dominates all other plasma motion. Then it is a simple matter to determine the growth rate and the spatial eigenfunction for the fastest growing mode associated with a given equilibrium. This determination is our primary objective.

It should be kept in mind that the eigenfunction analysis is used only for the interpretation of our results and not in the process of the computation itself.

Now consider the Fourier analysis of the perturbation. This step becomes an advantage only if the Fourier components evolve independently of each other -- only if there are no convolution integrals in the equations. This advantage is fulfilled if we use the linearized system and if we consider a Fourier decomposition only along the ignorable coordinate of the equilibrium. Given these conditions, and assuming the existence and convergence of the Fourier decomposition, we need to consider only one Fourier harmonic, characterized by the wave number k, at a time. By doing this, we reduce the computation to two spatial dimensions with an enormous saving of computer space and time as discussed below.

a) Linearization:

We linearize the equations around a given stationary equilibrium represented by the variables p^0 and $\vec{B}^0$ ($\vec{v}^0 = 0$ is omitted); the equilibrium is formally defined as:

$$\nabla p^0 = \vec{J}^0 \times \vec{B}^0 \tag{7}$$

$$\vec{J}^0 = \nabla \times \vec{B}^0 \tag{8}$$

$$\nabla \cdot \vec{B}^0 = 0 \tag{9}$$

The perturbed state is uniquely represented by the seven variables

$$\vec{v}^1 , \quad \vec{B}^1 , \quad p^1$$

which are determined by the equations:

$$\rho^0 \frac{\partial}{\partial t} \vec{v}^1 + \nabla p^1 - \vec{J}^1 \times \vec{B}^0 - \vec{J}^0 \times \vec{B}^1 = 0 \tag{10}$$

$$\frac{\partial}{\partial t} p^1 + \nabla \cdot (p^0 \vec{v}^1) + (\gamma - 1)\, p^0 (\nabla \cdot \vec{v}^1) = 0 \tag{11}$$

$$\frac{\partial}{\partial t} \vec{B}^1 + \nabla \times \vec{E}^1 = 0 \tag{12}$$

$$\vec{J}^1 = \nabla \times \vec{B}^1 \tag{13}$$

$$\vec{E}^1 + \vec{v}^1 \times \vec{B}^1 = 0 \tag{14}$$

together with appropriate boundary conditions and initial values. Note that the size of the perturbation variables is immaterial; the perturbation of the pressure, for example, could be represented by $p = p^0 + \varepsilon p^1$ where the scale factor ε may be taken arbitrarily small so that $\varepsilon p^1 \ll p^0$ even for large values of p^1.

b) Fourier Transformation:

We consider one Fourier harmonic of the perturbation with wave length λ along the ignorable coordinate z of the equilibrium.

$$U^1(x,y,z) = \mathrm{Re}\left(U^1(x,y)\, e^{ikz} \right) \tag{15}$$

where $k = 2\pi/\lambda$. The two dimensional perturbation vector $U^1(x,y)$ must be complex since its individual components may have different phases along z. It follows that

$$\frac{\partial}{\partial t} U^1(x,y,z) = \mathrm{Re}\left(i\, k\, U^1(x,y)\, e^{ikz} \right) \tag{16}$$

Linearization and Fourier transformation reduce the initially posed problem, namely the solution of eight equations for the eight 3D quantities ϱ, $\vec{v}$, p, $\vec{B}$ = f(x,y,z,t) to the solution of seven equations for the seven 2D quantities $\vec{v}^1$, p^1, $\vec{B}^1$ = f(x,y,t). Even with the slight complication that these quantities are complex, and the fact that the equilibrium quantities have to be stored in addition to these perturbed quantities, the computation is greatly simplified. To illustrate this, we write the problem in the following schematic form:

nonlinear 3D problem	=	2D equilibrium	+	3D perturbation

$$\begin{Bmatrix} \varrho \\ \vec{v} \\ p \\ \vec{B} \end{Bmatrix}(x,y,z,t) = \begin{Bmatrix} \varrho^0 \\ 0 \\ p^0 \\ \vec{B}^0 \end{Bmatrix}(x,y,t) + \mathrm{Re}\left(e^{ikz} \begin{Bmatrix} - \\ \vec{v}^1 \\ p^1 \\ \vec{B}^1 \end{Bmatrix}(x,y,t) \right)$$

8 REAL variables (3D grid)		5 REAL variables	+	7 COMPLEX variables
		on a 2D grid		

If we use a grid with 20 meshpoints in each direction, we can estimate the storage requirements for the two alternatives:

3D:	V(20,20,20)	--> 8 000 numbers per variable	
	8 real var.:	64 000 numbers	--> 256 000 bytes
2D:	V(20,20)	--> 400 numbers per variable	
	5 real var.:	2 000 numbers	
	7 cplx var.:	5 600 numbers	
		7 600 numbers	--> 30 400 bytes

This example illustrates that the two-dimensional form requires only a tenth of the storage compared with the full 3D problem; furthermore the computation time is less by at least an order of magnitude.

2.3 Initial Boundary-Value Problem

The system of partial differential equations for the quantities

$$\vec{v}^1 \ , \ p^1 \ \text{and} \ \vec{B}^1$$

is listed in full detail in APPENDIX A.

Boundary conditions:

The boundary values were chosen to conserve energy and to isolate the system. The discussion of the energy balance (APPENDIX B) leads to the following boundary conditions:

$$p^1 = 0 \tag{17}$$

$$\vec{E}^1_{\parallel} = 0 \tag{18}$$

$$\nabla \cdot \vec{E}^1 = 0 \tag{19}$$

The analytically equivalent form $\vec{v}^1_{\perp} = 0$ was not used for numerical reasons. Eq.(19) is used to determine $\vec{E}^1_{\perp}$ at the wall. The alternative of extrapolating $\vec{E}^1_{\perp}$ to the wall gave the same numerical results for the growth rate. However, Eq.(19) implies zero charge at the wall which seems physically reasonable.

Initial conditions:

A standard initial condition was designed to excite any choice or all of the m= 0, 1, 2, 3 modes. The velocity field was perturbed with a pattern resembling the radial displacement of these modes as they appear in known circular cylinder cases; the $\vec{B}^1$ and p^1 fields were initially set equal to zero. The choice of B^1 initially equal to zero ensures $\nabla \cdot \vec{B} = 0$ and it ensures that the perturbed state has the same topology as the equilibrium state.

3. Numerical Solution

In this section we shall describe the numerical methods of solution; the reader who is not interested in these technical details may skip to the results in section 4.

3.1 Calculation of the Equlibrium

Any equilibrium satisfying the basic equilibrium equations (7-9) can be used as the input data for our instability program provided there is no fine structure on the scale of the grid. However, if the wall is not a flux surface for the equilibrium, or if the pressure is not zero at the wall, care must be taken in choosing the boundary conditions for the perturbations when conservation of energy is desired.

For straight cylinders and axisymmetric toroids, it is convenient to introduce the poloidal flux function satisfying

$$\vec{B}^0 = \nabla\psi \times \hat{z} + B^0_z \hat{z} \qquad (20)$$

This relation assures $\nabla \cdot \vec{B}^0 = 0$. Then it follows from Eqs.(7-9) for a straight cylinder equilibrium with arbitrary cross section that

$$p'(\psi) + B_z B_z'(\psi) = J_z = -\nabla^2 \psi \qquad (21)$$

There is a similar formulation for axisymmetric toroidal equilibria. In general, no solution exists in the toroidal geometry if the spatial dependence of ψ or J_z is given and the functions $p(\psi)$ and $rB_\theta = I(\psi)$ are sought /12/. Hence we must specify $(p(\psi), I(\psi))$ and solve for $\psi(x,y)$, or equivalently $J_z(x,y)$, in order to have a single consistent equilibrium specification suitable for both straight cylinder and toroidal calculations.

In the program used here, the equilibrium is calculated by prescribing $(p(\psi), I(\psi))$, and the boundary values for ψ, and the value of the current density J_{zc} in the center of the domain. Von Hagenow's /13/ form of the Bunemann fast Poisson solver is used iteratively to find $\psi(x,y)$ in the rectangular domain. This procedure is so fast and trouble free that it is used routinely as an integral part of the instability code.

3.2 Solution of the Initial Boundary Value Problem

a) Calculation Mesh

The equilibrium quantities $Y^0 ::= \{p^0, \vec{B}^0\}$ are stored as REAL*4 variables; all perturbed quantities $Y^1 ::= \{\vec{v}^1, p^1, \vec{B}^1\}$ are represented by COMPLEX variables and complex arithmetic is used for their calculation. The variables are defined on a staggered 2D(x,y) grid as follows:

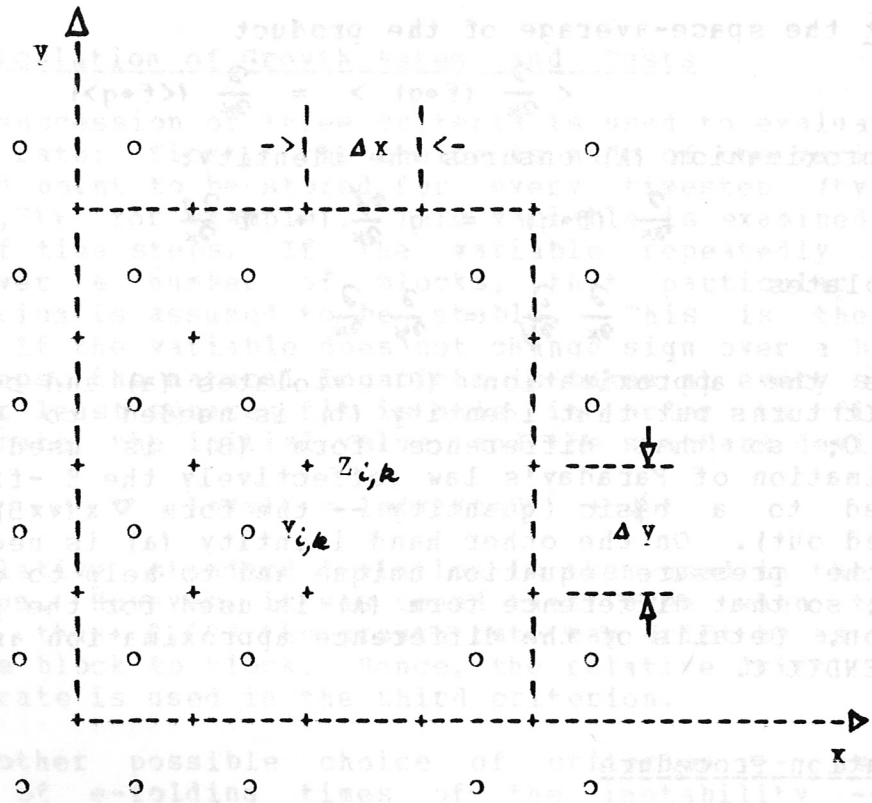

Fig.1 Calculation grid.

On the grid denoted by o, all the equilibrium quantities Y^0 and the perturbed velocities $\vec{v}^1$ are defined:

"o"-grid:

$$Y_{i,k} ::= \left\{ \begin{array}{lll} \varrho^0, & p^0, & v_x^1, \; v_y^1, \; v_z^1, \\ B_x^0, \; B_y^0, & B_z^0, & E_x^1, \; E_y^1, \; E_z^1, \\ J_x^0, \; J_y^0, & J_z^0, & J_x^1, \; J_y^1, \; J_z^1 \end{array} \right\}$$

On the grid denoted by +, the perturbed pressure and magnetic field are defined:

"+"-grid:

$$Z_{i,k} ::= \left\{ p^1, \; B_x^1, \; B_y^1, \; B_z^1 \right\}$$

b) Difference Equations

We have used a simple explicit scheme to integrate the partial differential equations forward in time. For the difference approximation we assume that all quantities are linear functions between the meshpoints. In particular for the approximation of spatial derivatives of products $f \cdot g$, we generally used the product of the space averages, i.e.:

$$\frac{\partial}{\partial x} (f \cdot g) \longrightarrow \frac{\partial}{\partial x} (\langle f \rangle \langle g \rangle) \qquad (A)$$

and not the space-average of the product

$$\left\langle \frac{\partial}{\partial x} (f \cdot g) \right\rangle = \frac{\partial}{\partial x} (\langle f \cdot g \rangle) \qquad (B)$$

The approximation (A) ensures the identity:

$$\frac{\partial}{\partial x} (f \cdot g) = g \frac{\partial f}{\partial x} + f \frac{\partial g}{\partial x} \qquad (a)$$

but violates

$$\frac{\partial}{\partial x} \frac{\partial}{\partial y} = \frac{\partial}{\partial y} \frac{\partial}{\partial x} \qquad (b)$$

whereas the approximation (B) violates (a) and conserves (b). It turns out that identity (b) is needed to preserve $\nabla \cdot \vec{B} = 0$; so that difference form (B) is used for the approximation of Faraday's law (effectively the E -field is elevated to a basic quantity -- the form $\nabla \times (v \times B)$ is not expanded out). On the other hand identity (a) is needed to make the pressure equation unique and to help to conserve energy; so that difference form (A) is used for the pressure equation. Details of the difference approximation are given in APPENDIX C.

c) Solution Procedure

The following flowchart shows in which order the several equations are integrated in time:

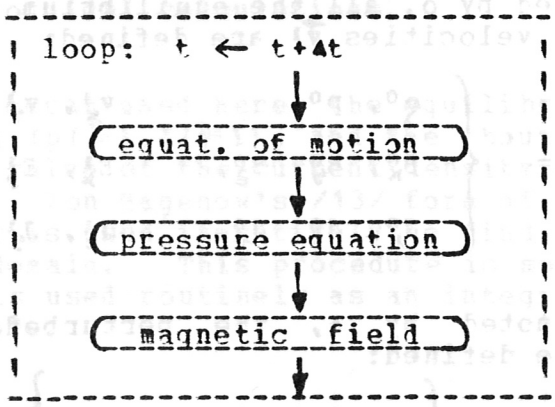

Fig. 2 Flow chart.

For the explicit scheme that we use, the maximum time step permitted by numerical stability considerations is determined by the maximum magnetosonic velocity over the equilibrium grid:

$$\Delta t \leq \Delta x / v_{MS} \tag{22}$$

An advantage of the linearized system is that this maximum time step is constant during a run. We used 0.8 of the maximum value.

3.3 Calculation of Growth Rates and Tests

A succession of three criteria is used to evaluate the growth rate: first, the choice is made of one variable at one grid point to be stored for every timestep (typically $Re(V_1(9,7))$ for example). This variable is examined over a block of time steps. If the variable repeatedly changes sign over a number of blocks, that particular plasma equilibrium is assumed to be stable. This is the first test. If the variable does not change sign over a block of time steps, the natural logarithm is taken at every step and a linear least squares fit is made in order to find the growth rate, the initial value, and the standard deviation.

$$\ln(v^1) = \ln(v^1(t=0)) + \gamma t \tag{23}$$

The relative standard deviation is then used in the second criterion. However, it was found that even when this is smaller than 0.001 the growth rate may drift by as much as 0.1 from block to block. Hence, the relative drift of the growth rate is used in the third criterion.

Another possible choice of criterion -- using the number of e-folding times of the instability -- was discarded because the criterion for convergence depends too much on the kind of initial conditions taken. More e-folding times are needed when very little of the mode is excited by the initial conditions than when the initial conditions are almost identical to the final mode.

At the end of each run, the differential growth rate

$$\gamma_\Delta = \frac{\Delta(\ln(v^1))}{\Delta t} \tag{24}$$

is examined over the whole spatial grid in order to make sure that only one eigenfunction remains. For well converged runs, γ_Δ is typically uniform to ten percent or so except in the corners or near the null points of the variable being examined. However, we found that the growth rate determined by the least squares fit generally converged long before the differential growth rate becomes uniform.

We call the unstable mode with the highest growth rate the "dominant mode" and ones with the lower growth rates the "subdominant modes". We used several techniques to find the subdominant modes:

There are generally a finite set of equilibrium conditions where the growth rates of two modes are the same. As we change the equilibrium conditions to cross this point, the final eigenfunction of the dominant mode can be used as the initial conditions of the next run to excite what is now the subdominant mode. In this way the growth rate curves can be followed under each other. Unfortunately, this technique breaks down as the disparity between the growth rates becomes large (as the equilibrium is changed). A little bit of the dominant mode is always excited.

Hence a second technique was devised which relies on the symmetry properties of the modes as they exist on equilibria with symmetries. For our equilibria, it was found that even and odd modes exhibit even or odd reflection symmetries across the midplane of the rectangular cross section. The parity of the symmetry condition is different for each variable but the parity of the collection of variables taken together as an eigenvector just flips as you shift your consideration from the even to the odd modes, or if the phase $(k \cdot z)$ of any given mode changes by 90^0 along the z axis. Since the transition between dominant and subdominant modes generally takes place between even and odd modes, the technique of forcing symmetry conditions upon the modes can be used to extend the study of modes as they become subdominant; (it also saves computer time). However, when there are large differences between the growth rates, this technique also breaks down. Modes with a 90^0 shift of phase along the z axis, relative to the modes which were deliberately excited, grow large enough to mask the subdominant modes.

Four checks of the program were made: First of all the time step was varied; the growth rate remains unaltered for time steps up to 0.8 of the maximum allowed by numerical stability (see Eq.(22)). Second, the growth rate remains the same to within 1% as the number of meshpoints is doubled from 18 to 34. Third, a form of energy conservation was considered. The full energy conservation is derived in APPENDIX B. A shorter conservation law of the linearized equations -- omitting the second order quantity v^2 -- was used instead so that the time derivative of the conserved quantity could be found explicitely using only the first order quantities. We found that the integral of this conserved quantity grows at a rate of just 1% of the kinetic energy. Finally, the favourable comparison made between our square cylinder results and circular cylinder results are discussed in section 4.1.

4. Results

Up to this point we have described the initial boundary-value method as it applies to finding MHD instabilities. Now we shall present a detailed picture of the instabilities that we have found -- first by examining individual examples, then by plotting the growth rates collected over many runs as a function of the equilibrium parameters, and finally by collecting the marginal points deduced from many graphs of the growth rate and plotting the marginal current density or q-value or β as a function of b/a and k•a.

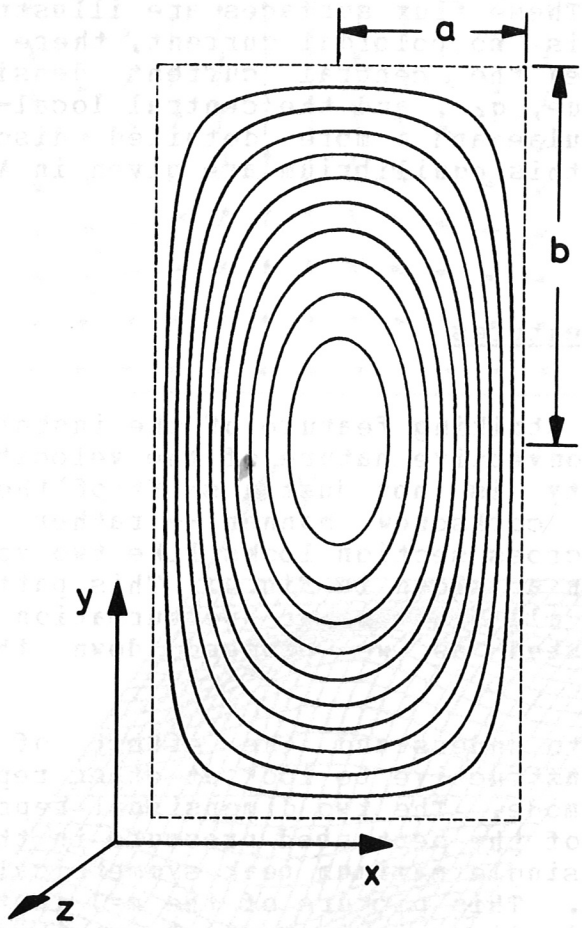

Fig. 3 A cross section of the equilibrium domain and the flux surfaces ($p'(\psi) = J_{zc}\psi/\psi_c$).

Historically, we first studied an equilibrium with uniform longitudinal current density. But all the results that are presented in this report were derived using the

equilibrium specified by

$$p'(\psi) = J_{zc}\psi/\psi_c \,, \quad \psi(\text{wall}) = 0$$
$$B_z^0 = 1 \,, \quad \rho^0 = 1 \qquad (25)$$

filling a straight rectangular cylinder. Here, the longitudinal current density is mildly concentrated in the center of the domain and is zero at the walls. This has the advantage of keeping the instabilities away from the walls but generally keeping them broad enough to make effective use of most of the grid. Furthermore, this equilibrium has a number of simplicities not found in the uniform current model -- for example all the nested flux surfaces have the same ratio of major to minor axes (vertical to horizontal dimensions). These flux surfaces are illustrated in Fig.1. Since there is no poloidal current, there is a one-to-one relation between the central current density, J_{zc}, the central q-value, q_c, and the central local-β-value, β_c. All these formulae and a more detailed discussion of the properties of this equilibrium are given in APPENDIX D.

4.1 General Features

The most striking feature of the instabilities we have found is the convective nature of the velocity field. The m=1 instability is not just a shift of the plasma towards the wall in a corkscrew manner -- rather it is a flow pattern whose cross section looks like two vorticies rolling off each other as shown in Fig.4. This pattern, as well as the pattern of all the other perturbation variables, is helically twisted as we proceed down the tube in the z-direction.

In order to understand the effect of this velocity field, it is instructive to look at other representations of the same m=1 mode. The two dimensional representation of a cross section of the perturbed pressure in the lower part of Fig.4 shows a single maximum peak symmetrically opposed to a minimum valley. This picture of the m=1 instability can be brought more in line with our usual intuitive picture if we look at contour plots of the same perturbed pressure and then the corresponding contour plots of the sum of equilibrium and perturbed pressure shown in Fig.5. (The numbers 5 to 9 represent positive values and 4 to 0 represent negative values of the variable). It is clear from Fig.5 that the double vortex pattern of Fig.4 results in a helical shift of the plasma as well as convection of material around the closed flow pattern (and in general some compression).

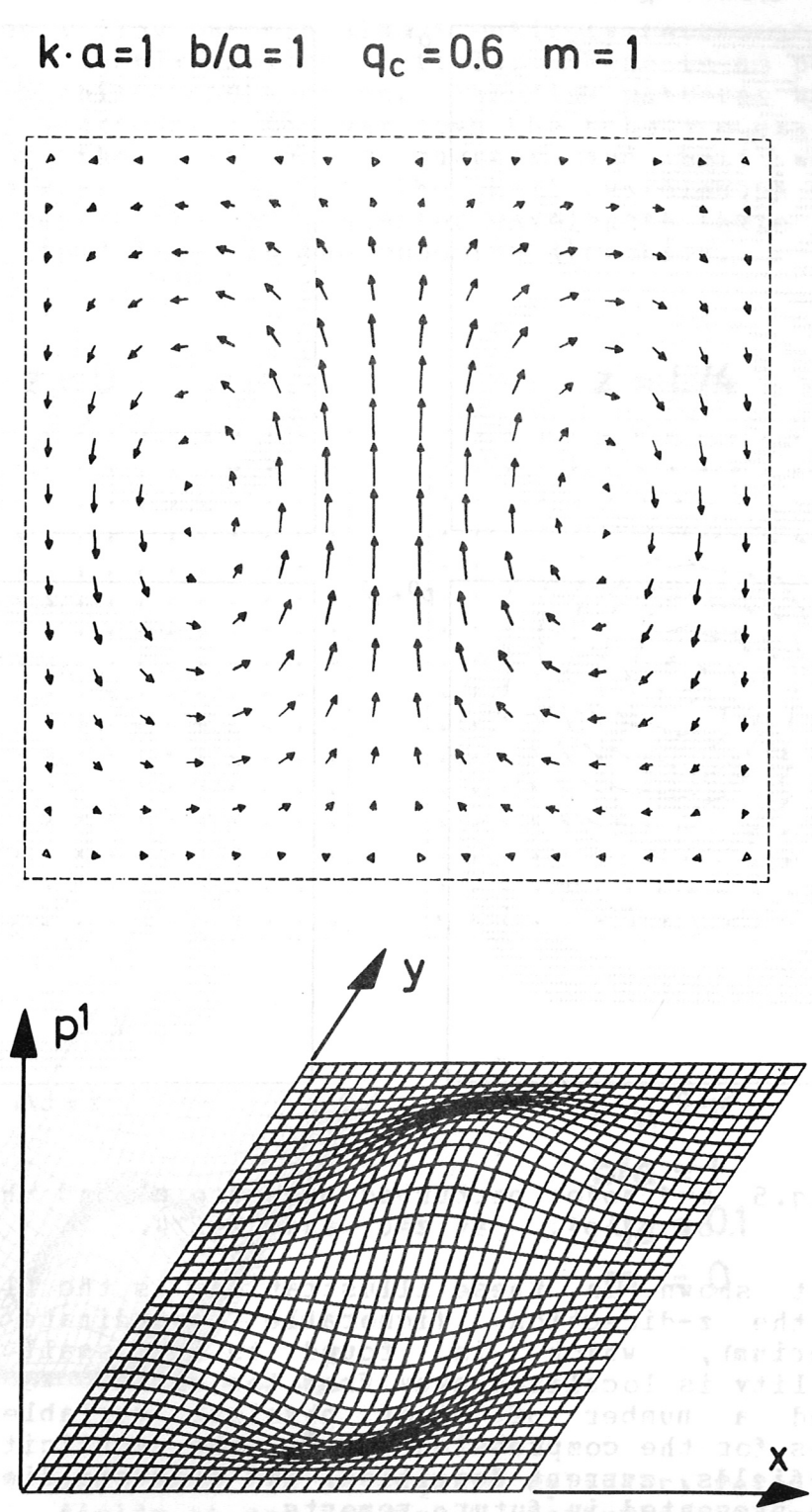

Fig.4 Typical m=1 mode in a square cylinder: k•a=1, q_c = 0.6; velocity field and perturbed pressure.

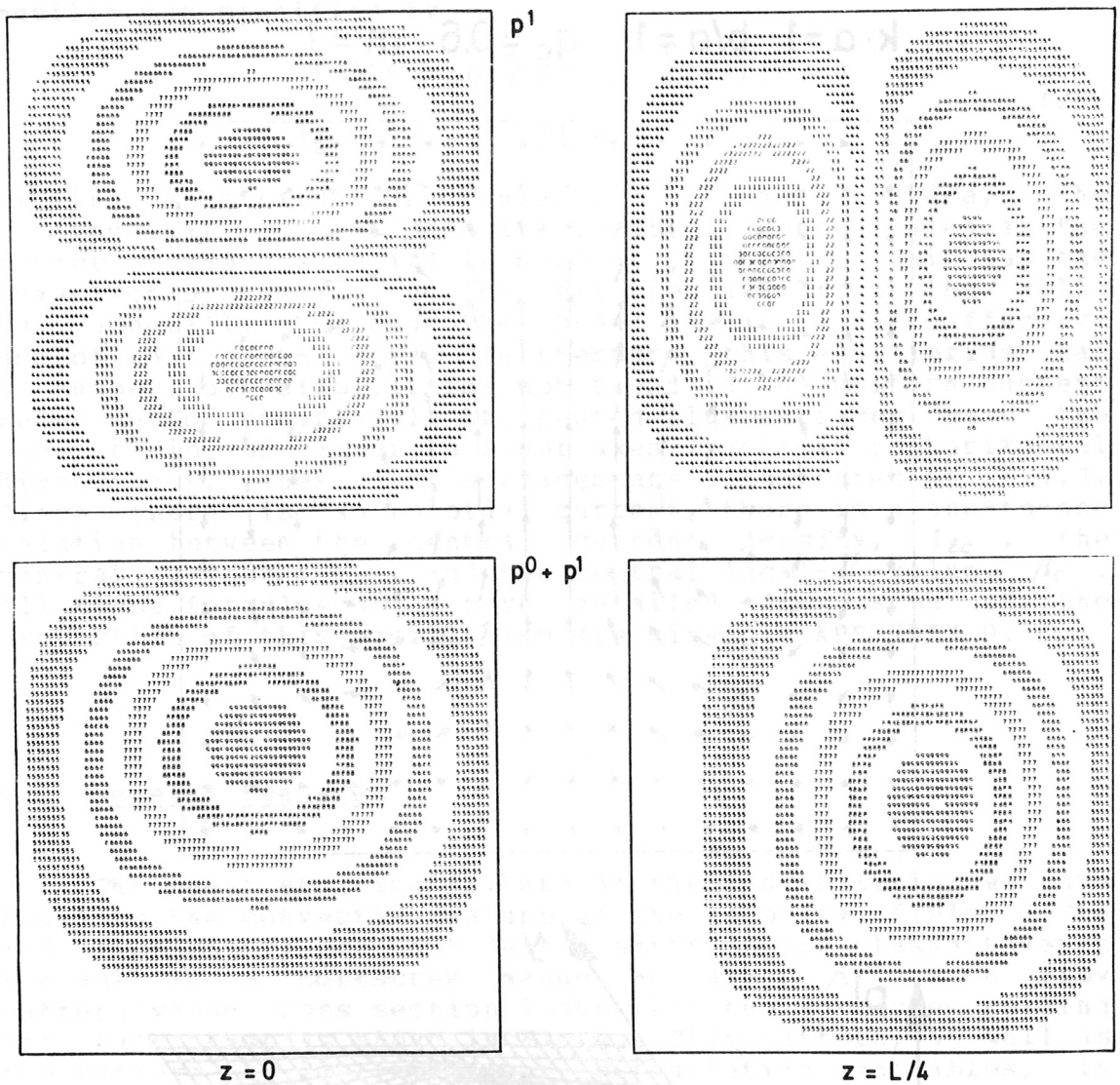

Fig.5 m=1 mode; perturbed pressure p^1 and the sum of p^0+p^1, at z=0 and z=L/4.

Not shown in these illustrations is the flow pattern along the z-direction (ignorable coordinate of the equilibrium), which is found to be small when the instability is localized away from the walls. We have also examined a number of other physical variables such as measures for the compression ($\nabla \cdot \vec{v}$), the vorticity ($\nabla \times \vec{v}$), the B-fields, current densities, and electric fields, which will be presented in future reports.

A cross section picture of the m=0 mode is shown in Fig.6 for both the z=0 cross section and the z=L/4 section (a quarter of a wavelenght down the tube). At z=0 there is clearly compression towards the center of the box, which is evident from both the velocity field and the perturbed pressure profile. In this cross section there is almost no z-velocity. However, a quarter of a wavelength down the

tube we see a flow pattern almost entirely representing flow along the tightly coiled B-field. There is no perturbed pressure in this cross section. The flow patterns half way and three quarters of the way down the tube are exactly the negative of the patterns a quarter and half way down respectively -- i. e. at the half wavelength there is expansion and at the three-quarter wavelength there is flow along the field lines in the opposite direction.

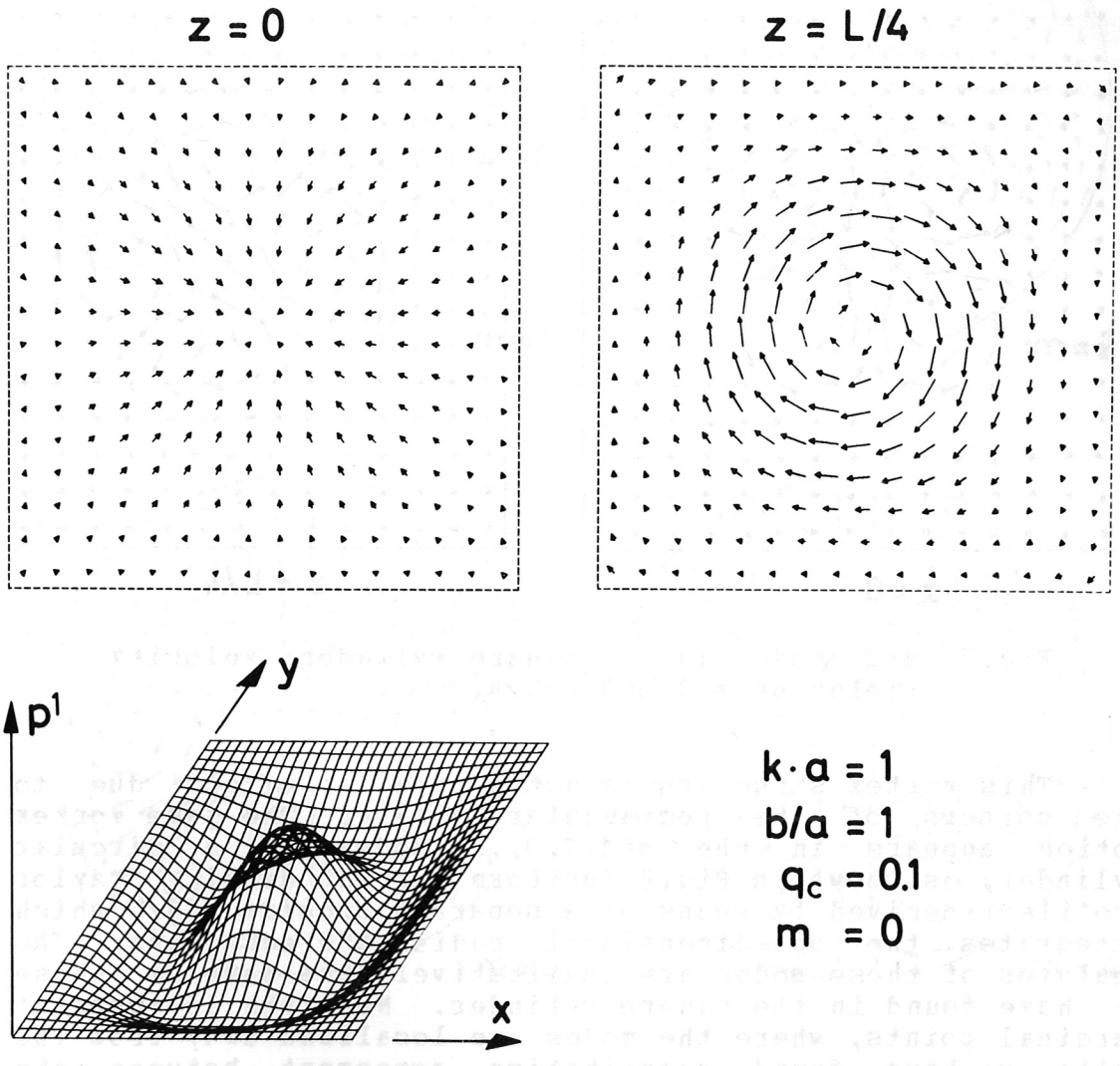

Fig. 6 m=0 mode in a square cylinder; velocity fields at z=0 and z=L/4, perturbed pressure at z=0.

The velocity field of the m=2 mode is shown in Fig. 7 for cross sections at z=0 and z=L/4. There are clearly four convective cells which have a helical pitch which brings them half-way around as we proceed the full length down the tube. In general, we observed a helical pitch of 1/m for

the higher m-modes. This m=2 mode was difficult to excite in the square cylinder because it is fairly localized and because it is unstable over only a narrow range of current densities.

$k \cdot a = 1 \quad b/a = 1 \quad q_c = 2.0 \quad m = 2$

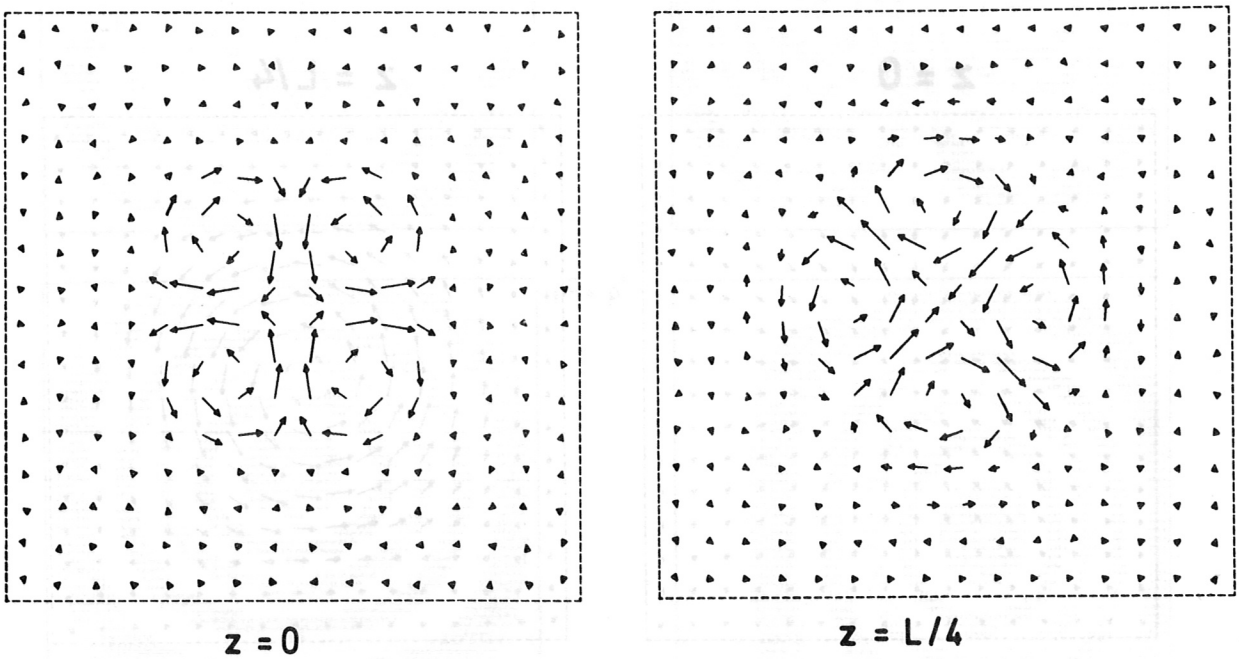

Fig.7 m=2 mode in a square cylinder: velocity fields at z=0 and z=L/4.

This vortex structure is not a peculiar effect due to the corners of the rectangular domain. The same vortex motion appears in the m=1,2,3,... modes of a circular cylinder, as shown in Fig.8 (uniform current density "Taylor profile") derived by means of a separate program /14/, which integrates the one-dimensional radial MHD equations. The features of these modes are qualitatively the same as those we have found in the square cylinder. Near the low-current marginal points, where the modes are localized away from the walls, we have found quantitative agreement between the growth rates of the uniform current square cylinder and the circular cylinder using results first given to us by Sakanaka /15/. Note in Fig.8 that each azimuthal mode m is characterized by 2m vortex cells. Also there exist distinct radial modes (not shown) which are characterized by nodes in the radial velocity. These higher radial modes are less interesting to us than the fundamental mode because their growth rates are always smaller and because they are more localized.

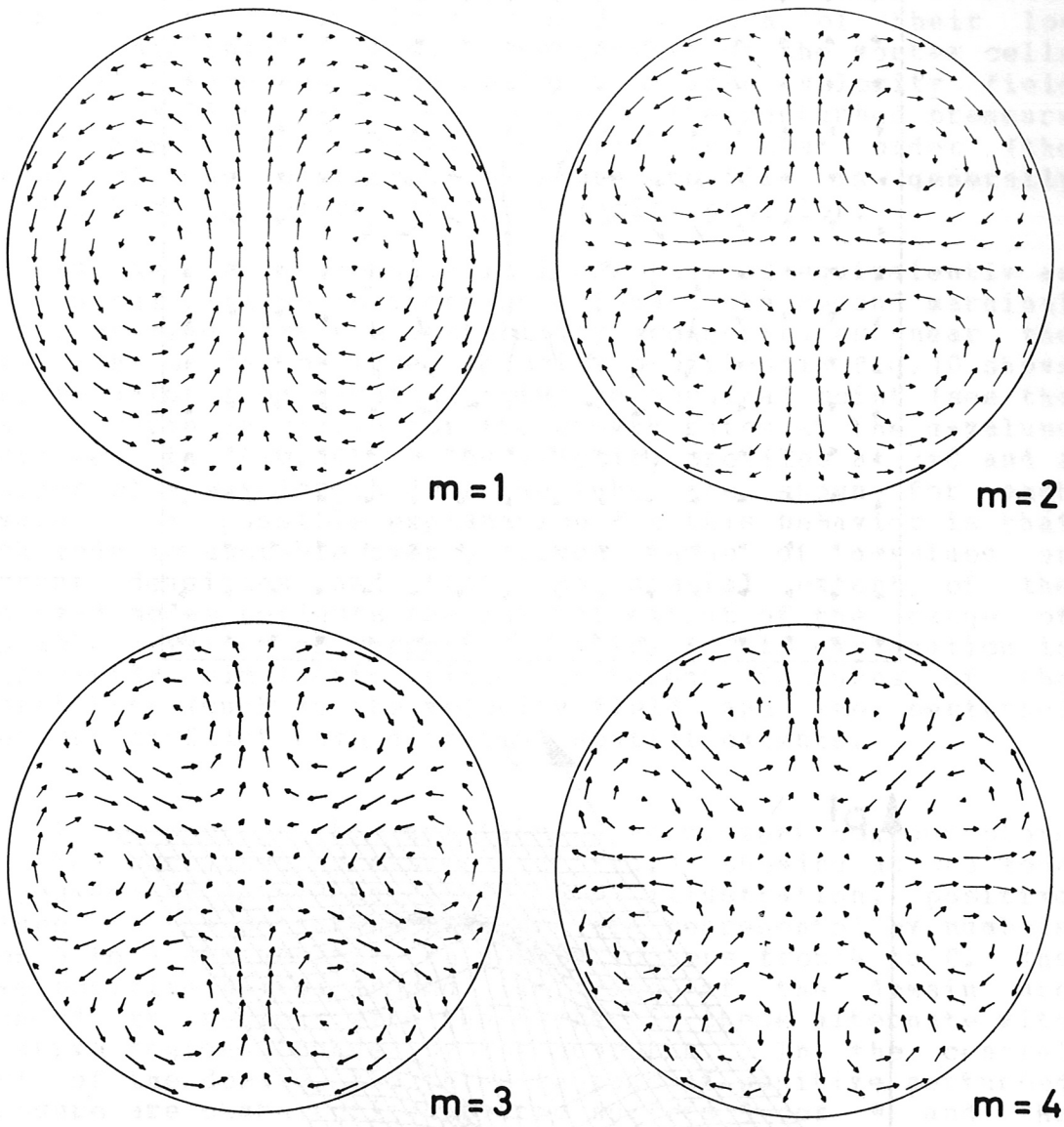

Fig. 3 Circular cylinder with uniform current density, B^0-field, and mass density; cross sections of the velocity fields for typical m= 1,2,3 and 4 modes.

Before looking at how these modes are altered by elongating the cross section, let us consider how the spatial extent of the instabilities changes as the current density (and growth rate) are changed.

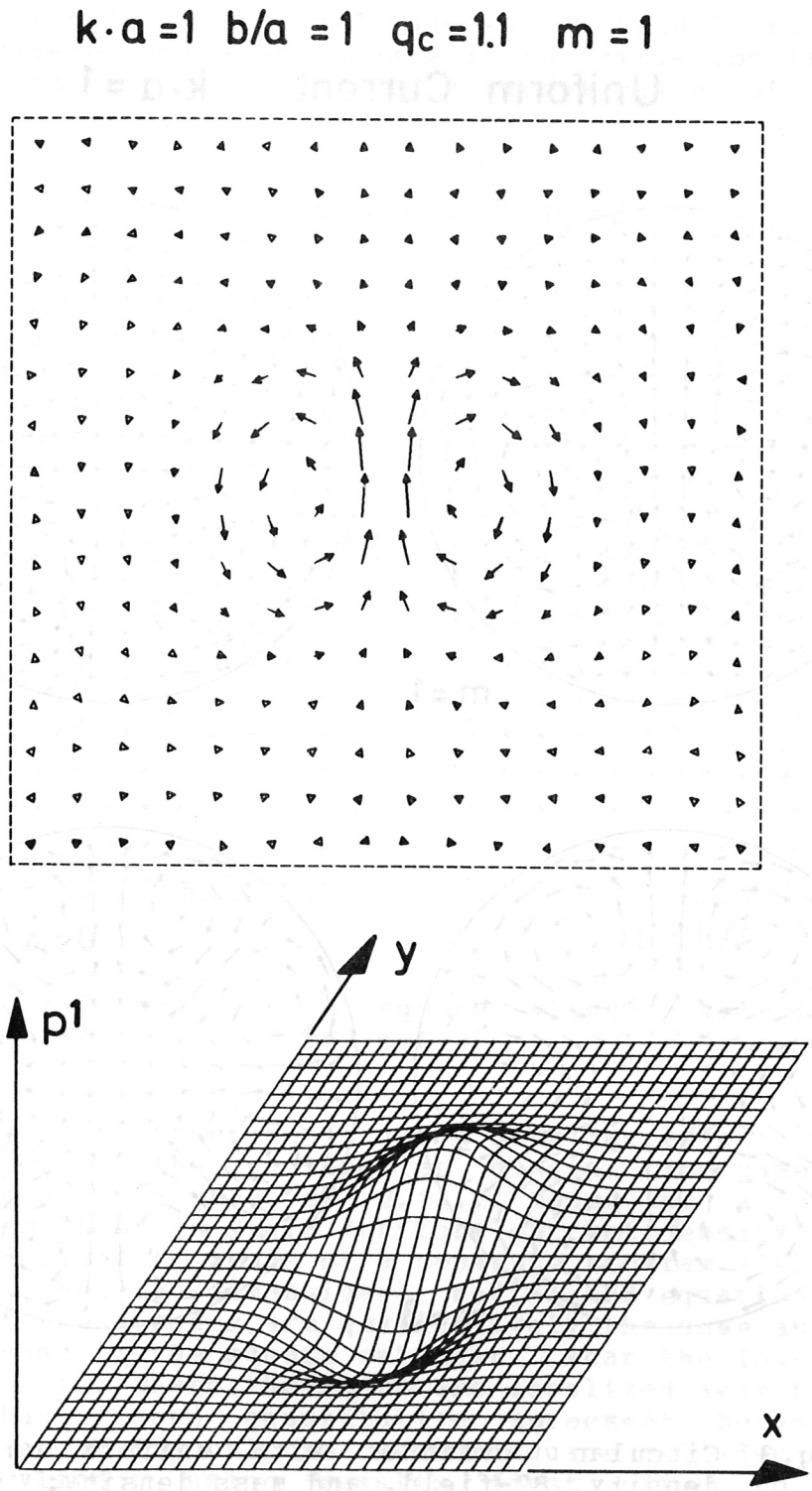

Fig.9 m=1 mode near the marginal point; velocity field and perturbed pressure; square cylinder, k•a=1.

The m=1 mode that we showed in Figs.4 and 5 is typically the way the mode appears far from the marginal points. But as we decrease the current density close to the marginal point, where the growth rate goes to zero, the same mode concentrates near the center of the domain as shown in Fig.9. This behavior is typical of all the observed modes as the current density is decreased to each of their low current marginal points. The centers of the vortex cells move closer together, the extent of the velocity field becomes smaller, and the peaks of the perturbed pressure profile move closer together, roughly in that order (the extent of the perturbed pressure profile is generally broader than the extent of the velocity profile).

As the current density is increased, or equivalently as the central q-value is decreased, toward the second marginal point, we find that the instability concentrates near the wall. The series of three velocity profiles in Fig.10 shows this behavior from marginal point to marginal point (see the b/a=1.5 curve in Fig.18 for the growth rates at the q-values indicated in Fig.10). The velocity profiles at z=0 and a quarter of a wavelength down the tube are shown for each q-value. A possible explanation for this behavior is that each mode is unstable over a given range of q-values or current densities and that the spatial extent of the observed modes reflects the spatial extent of the range of unstable q-values or current densities. This explanation is necessarily simplistic since different features of the instability (such as the velocity field and the perturbed pressure profile) have different spatial extents.

In support of this hypothesis, we present contour plots of the perturbed pressure in Fig.11 showing an m=3 mode surrounded by an m=5 mode. In this illustration, positive values of the perturbed pressure are represented by numbers from 5 to 9 and negative values by numbers from 4 to 0. The five positive maxima around the edge of the domain are bounded by regions with the number 5; these alternate with negative regions bounded by the number 4. In the central part of the domain, the three regions of positive perturbed pressure are characterized by the numbers 8 or 9 and the negative regions by the numbers 1 or 0. Hence we conclude that we are observing an m=3 mode surrounded by an m=5 mode. (This configuration shows up better on the perturbed pressure plots because the very small velocity fields associated with this m=5 mode produce a perturbed pressure which is magnified by the steep gradient in the equilibrium pressure near the wall.) The local q-value (for each flux surface) increases from 3 in the center to infinity at the wall. The m=3 mode is unstable at the central q-value of 3 but is believed to be stable at much higher q-values. The m=5 mode is expected to be unstable for q-values in the neighbourhood of 5.

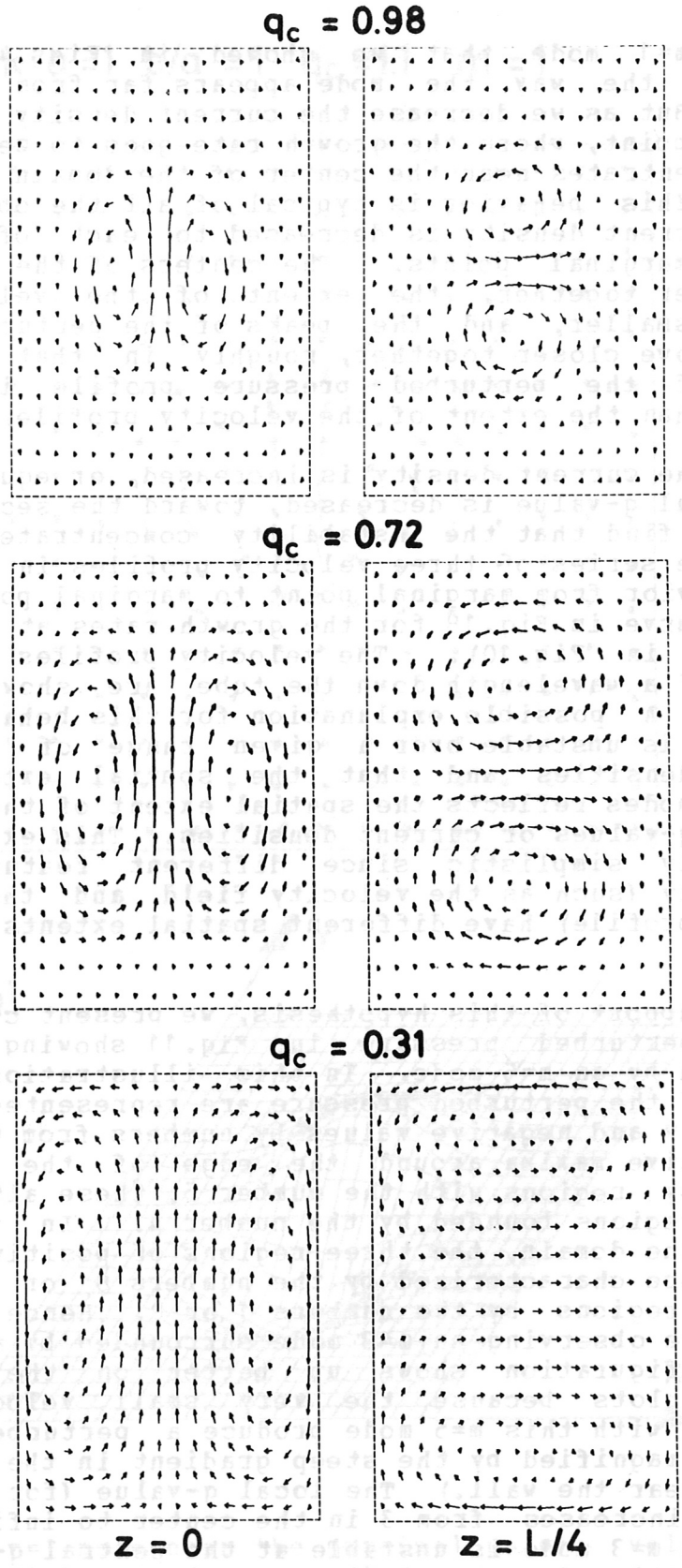

Fig.10 Series of m=1 modes for a rectangular cylinder, b/a=1.5, k•a=1/2.

Hence the hypothesis is supported; but the evidence does not tell us which equilibrium parameter is responsible for the localization -- e.g. the local q-value or current density or other related parameter. Also we expect that the structure shown in Fig.11 is at the limit of the resolution for the 18 by 34 grid that we used in this run.

$k \cdot a = 1 \quad b/a = 6 \quad q_c = 3.0 \quad m = 3, 5$

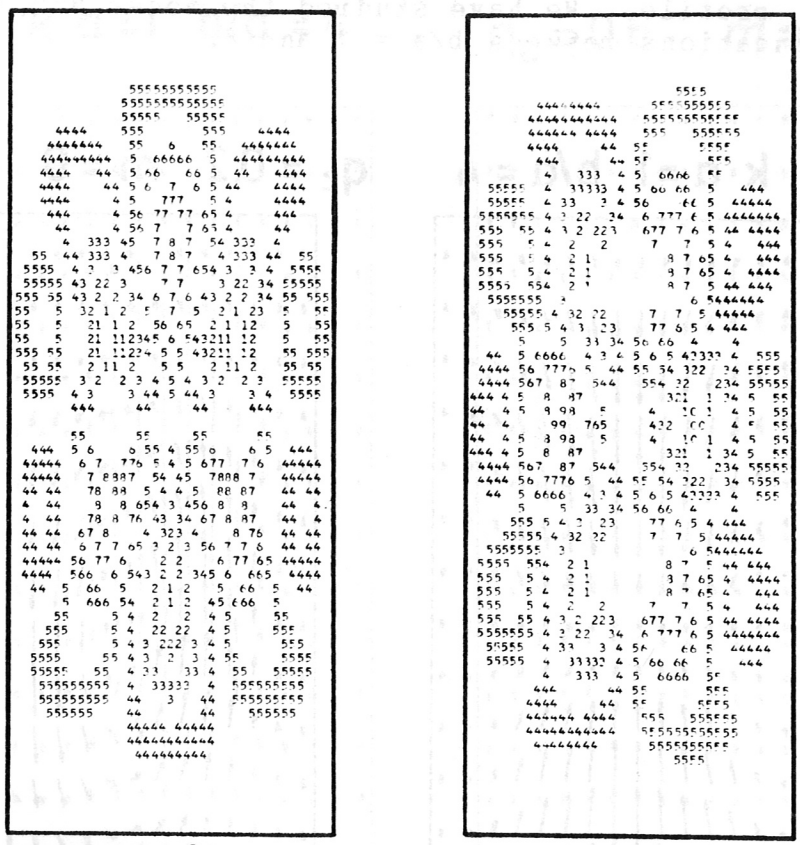

z = 0 z = L/4

Fig.11 Perturbed pressure p^1; rectangular cylinder, k•a=1; m=3 surrounded by m=5 mode.

However, there is evidence that the spatial extent of the instabilities is related to the spatial form of the q-value (rotational transform) rather than that of the current density or other equilibrium parameters. In case of a highly elongated (b/a>2) rectangular cylinder filled with uniform longitudinal current, the rotational transform has a steep maximum near the walls and a broad minimum through the center. We find that the m=1 mode near the low-current marginal point is spatially concentrated near the ends of the domain around the maxima of the rotational transforms,

(while the current density, mass density and B^0 field are all uniform). However this observation must be investigated further in order to isolate the effects of shear, radial dependence of b/a, and other characteristics of elongated equilibria.

Now we shall examine the effect of elongation on the spatial form of the observed fixed-boundary instablities. As in the circular and square cylinder, there are distinct azimuthal modes, each characterized by 2m vortex cells of the velocity field and m positive maxima of the perturbed pressure profile. We have studied the modes m=0, 1, 2, and 3 using elongations between b/a = 1 and 8.

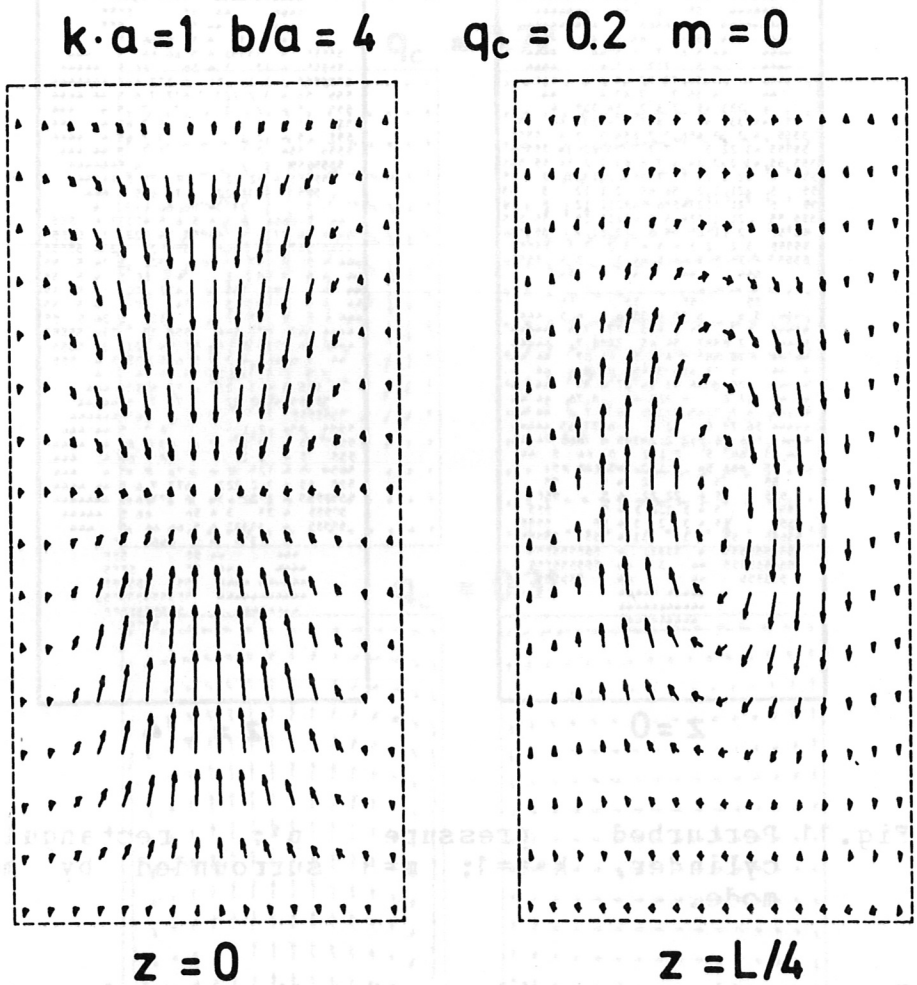

Fig. 12 m=0 mode for a rectangular cylinder, b/a=4, k•a=1, q_c = 0.2, cross sections of the velocity field at z=0 and z=L/4.

A typical example of an m=0 mode is shown in Fig. 12. For the purposes of presentation, the four-to-one rectangular domain is represented here by a two-to-one plot.

The velocity vectors have been normalized so that the maximum x or y component over the whole grid is 0.9 of the minimum grid spacing. The components of the velocity vectors are all in scale for both cross section views.

Note that the motion from side to side, for this m=1 mode, is much less than the motion from top to bottom. The perturbed pressure plots (not shown) look like an elongated version of the corresponding square cylinder mode.

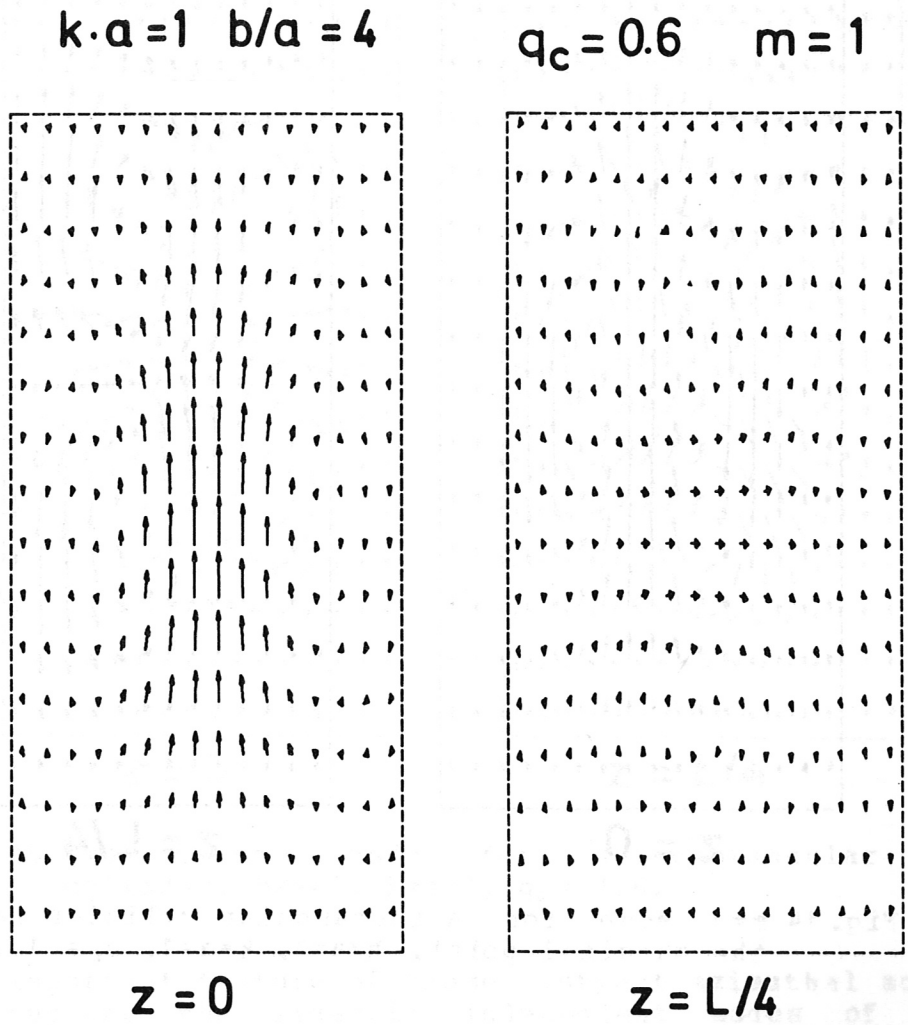

Fig. 13 m=1 mode for a rectangular cylinder, b/a=4, k•a=1, q_c = 0.6.

Two examples of the m=1 mode are presented in order to show how the mode changes as the low-current (high q-value) marginal point is approached. Fig. 13 shows the m=1 mode far from the marginal point. Almost all the motion is in the z=0 plane, where the plasma shift is vertical. However the magnitude of the maximum perturbed pressure (not shown) is nearly the same in the two cross sections. This is consistent with the velocity picture since the gradient of

the equilibrium pressure is much steeper from side to side than it is from top to bottom. Nevertheless, the predominant displacement of the plasma is planar, as would result from the sum of an m=1 and m=-1 helical displacement.

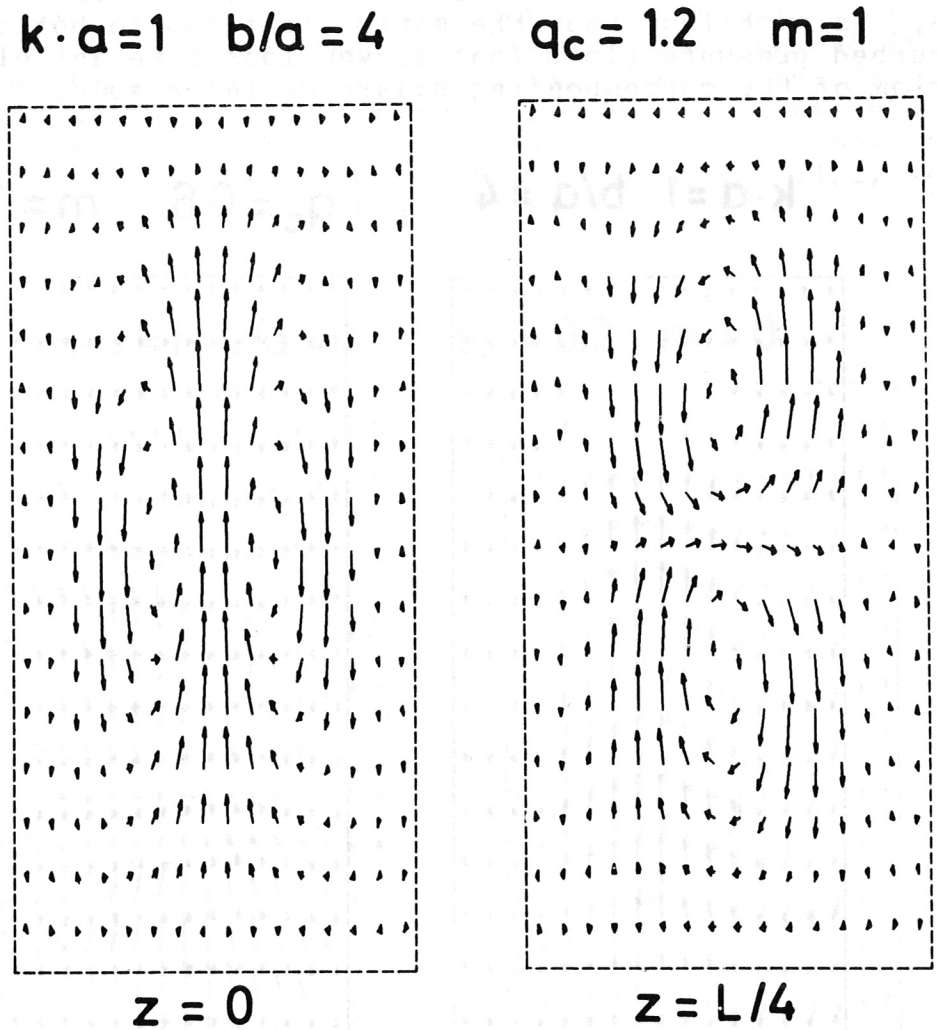

Fig. 14 m=1 mode for a rectangular cylinder near the marginal point, b/a=4, k•a=1, q_c = 1.2.

The picture looks quite different for current densities near the marginal point, as shown in Fig. 13. There is much more side-to-side motion in the z=L/4 cross section. The centers of the vortex cells are closer together, but the overall extent of the mode does not appear to be more localized. The peaks of the perturbed pressure (not shown) are localized near the ends of the z=0 cross section and they assume the form of a ridge and long valley along either side of the z=L/4 cross section. This behavior might be explained by the fact that the spatial profile of the q-value becomes more flat as the cross section is elongated for our choice of equilibrium (see Fig. 22 in APPENDIX D).

A typical example of the m=2 mode for elongated cross sections is shown in Fig.15. As the low-current marginal point is approached, the mode concentrates in the center of the domain as expected.

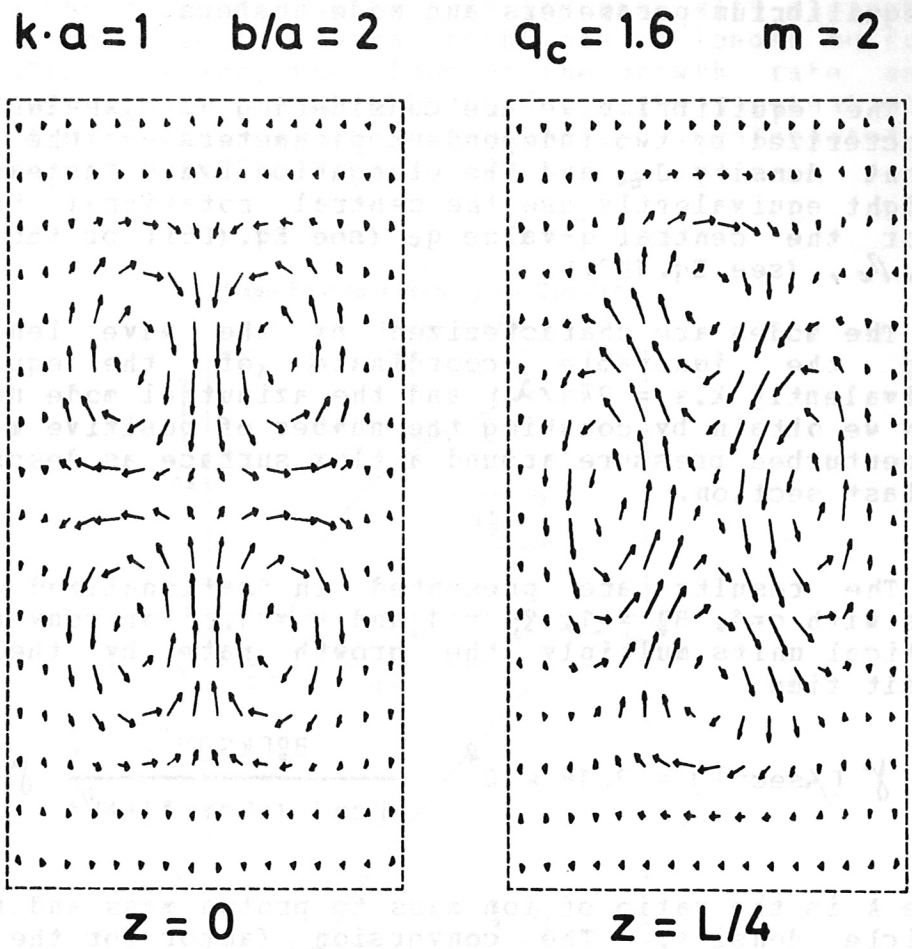

Fig.15 Typical m=2 mode for a rectangular cylinder, b/a=2, k•a=1, q_c = 1.6.

An important feature of these distinct azimuthal modes is that they are the linearly independent modes of the equations (there is also a spectrum of linearly independent stable modes). Different azimuthal modes (generally with different growth rates) are found to exist simultaneously for equilibria with elongated cross sections. It is possible to excite a mode with lower growth rate, and to observe it alone, by carefully choosing the initial conditions. There is none of the "mode-mode coupling" which is discussed by those researchers /16/, /17/, who are considering Fourier "modes" of the eigenfunction relative to a particular choice of azimuthal coordinate. The modes we are observing are independent of each other and are independent of the coordinate system used.

4.2 Growth Rates

Up to this point we have considered the instability features as they are observed in individual runs. Now we shall present the instability growth rates as a function of the equilibrium parameters and mode numbers.

The equilibrium we are considering (see APPENDIX D) is characterized by two independent parameters -- the central current density J_{zc} and the elongation b/a. Instead of J_{zc} we might equivalently use the central rotational transform ι or the central q-value q_c (see Eq.(D6)) or the central beta, β_c, (see Eq.(D7)).

The modes are characterized by the wave length λ, along the ignorable coordinate of the equilibrium (equivalently $k \cdot a = 2\pi a/\lambda$) and the azimuthal mode number m which we obtain by counting the number of positive maxima of the perturbed pressure around a flux surface as described in the last section.

The results are presented in rationalized Gaussian units with c=1, $B_z^0 = 1$, $\rho^0 = 1$ and a = 1. For conversion to practical units multiply the growth rate by the Alfven transit time

$$\gamma\,[\mu\text{sec}^{-1}] = 2.18 \times 10^{8}\ \frac{B_z^0[\text{kG}]}{a[\text{cm}]\ (n[\text{cm}^{-3}] \cdot A)^{1/2}}\ \gamma \qquad (26)$$

where A is the ratio of ion mass to proton mass and n is the particle density. The conversion factor for the current density is

$$J_z\,[\text{A/cm}^2] = 796.\ \frac{B_z^0[\text{kG}]}{a[\text{cm}]}\ J_z \qquad (27)$$

Our investigation began with the very short wave length, $\lambda = 2\pi a$, (k·a=1). For short wavelengths, we expect relatively broad ranges of instability and large growth rates -- comparable to the Alfven tansit time across the plasma column. The growth rates for the m=1, 2, and 3 modes are shown in Fig.16 as a function of the central current density for the elongations b/a= 1, 2, and 4. The first surprising feature is that the high current marginal point could not be found in many cases. For example, ~~for b/a=8~~ the growth rate of the m=1 mode is 10^9 for a current density of 10^{10} and b/a= 8. On the other hand, the m=2 mode is unstable over only a narrow range of current densities for b/a=1. It is very difficult to excite because its growth

rate is low and it is spatially localized. This situation changes dramatically as we elongate the cross section of the cylinder. The range of instability for the m=2 and 3 modes rapidly spread out and they became much easier to excite because they are less localized in space (as well as J_{zc}). The domains of instability merge with those of the lower modes and the maximum growth rates increase with elongation until the high current marginal point can no longer be found (see Fig. 17). However, the slope of the growth rate as a function of J_{zc} in the neighbourhood of the marginal point goes to a finite limit as the cross section is elongated (we have gone up to b/a= 8).

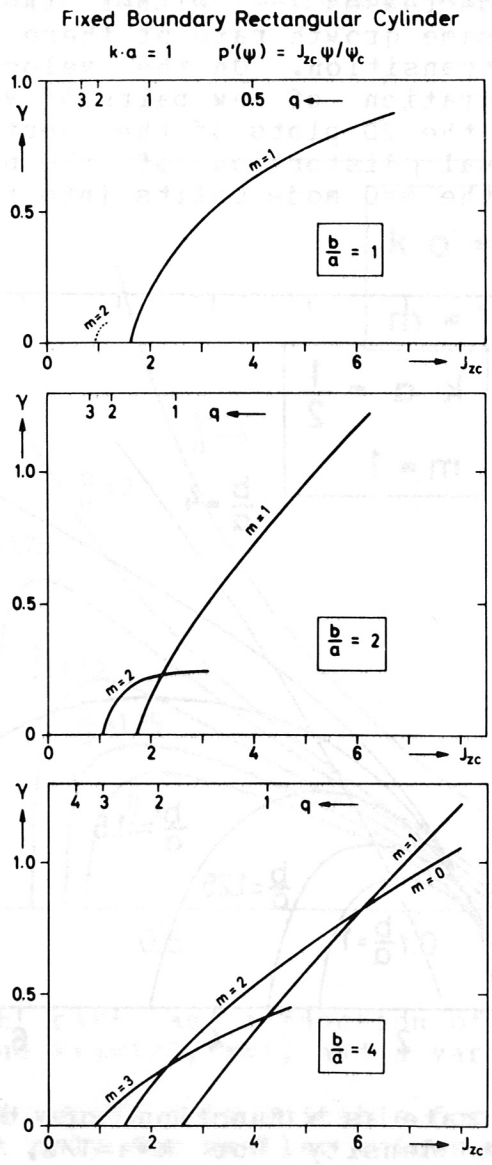

Fig. 16 Growth rate as a function of the central current density for k•a=1, b/a= 1,2,4 and m= 1,2,3.

The b/a=2 and 4 parts of Fig.16 show clear examples of several modes existing simultaneously under the same equilibrium conditions. It was possible to separate even and odd modes by using symmetry conditions but we found no way to suppress the m=3 mode for example in order to follow the m=1 mode down the marginal point for b/a>3 . Because of this effect, we were completely unable to estimate the m=1 marginal point for b/a>6 . As the cross section is elongated, it appears that successively higher modes take over as the dominant mode which masks all the lower modes under it.

One more effect indicated in Fig.16 is that the m=0 mode appears to make a smooth transition over to an m=2 mode as the current is decreased -- either they are distinct modes with the same growth rate or there is only one mode which undergoes a transition. On the velocity plots this appears as a migration of new pairs of vortex centers in from the wall. On the 2D plots of the perturbed pressure, there is a gradual distortion of the p¹ surface as the single maximum of the m=0 mode splits into two.

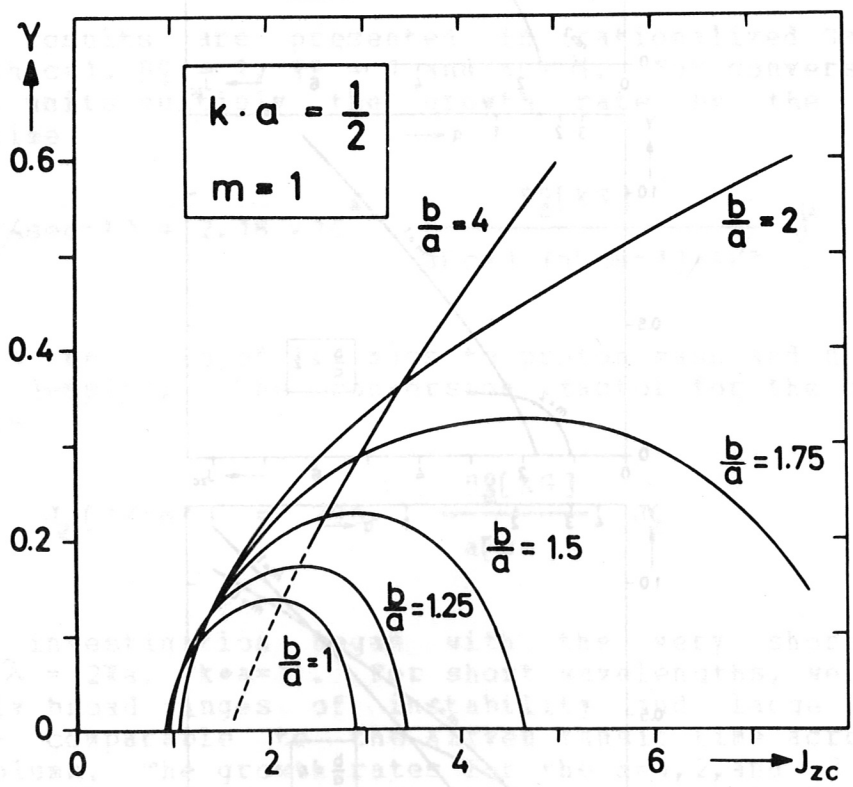

Fig. 17 Growth rate as a function of the central current density for k•a=1/2, m=1, and a variety of elongations b/a.

A detailed study of the behaviour of the m=1 mode for b/a between 1 and 2 and k•a=1/2 is shown in Fig.17 for γ versus J_{zc}. For this longer wavelength (k•a=1/2) the m=1

high-current marginal point could be found for the square cylinder but the growth rates are an order in magnitude smaller than the k•a=1 case. Note how the low-current marginal point remains nearly constant while the high-current marginal point rapidly expands out of the range, and apparently to infinity, as b/a is increased between 1 and 2. The low-current marginal point begins to change appreciably only when b/a is increased to 4 and above.

In Fig.18 we see the clearly nested form of the growth rate curves, for k•a=1/2, plotted as a function of the central q-value. Note that the low-current marginal points of Fig.17 correspond to the high-q marginal points of Fig.18. The separation of the marginal points is clearer in Fig.18.

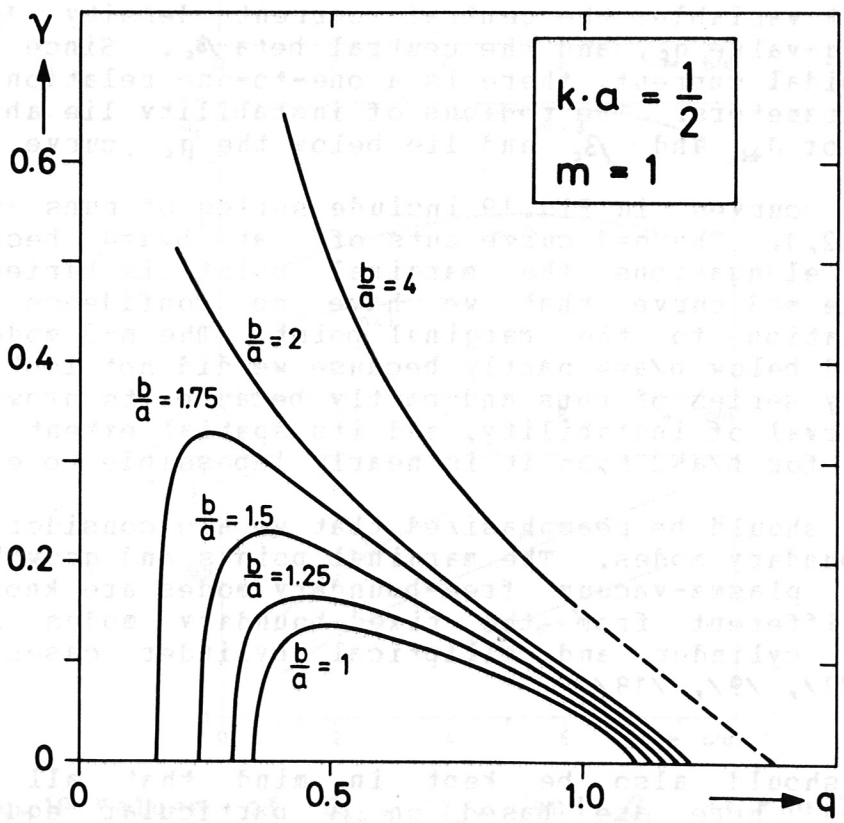

Fig. 18 Growth rate as a function of the central q-value k•a=1/2, m=1, and a variety of b/a.

The plot of γ versus q is suitable for extrapolating to the marginal point only for smaller values of b/a and k•a. When either of these parameters is large, the γ versus q curve appears to join the $\gamma = 0$ axis tangentially. We generally need γ versus J_{tc} plots to determine the best estimate of the marginal point.

4.3 Marginal Points

The next level of data reduction is to tabulate the marginal points, estimated by extrapolation of the growth rate curves, and to present a picture of how the marginal equilibrium parameters vary relative to each other: for example how does the marginal current density vary with b/a and k•a. We shall consider the low current marginal points for each m-mode separately. It should be kept in mind that the lower-m marginal points are generally buried under the higher-m growth rates. It makes sense to present the lower-m marginal points only because there is reason to believe that the higher-m modes are less dangerous and are selectively suppressed by non-ideal MHD effects.

In Fig.19 the marginal points for the m= 1,2, and 3 modes are plotted as a function of b/a for fixed wavelength (k•a=1). Three equivalent choices are made for the dependent variable: the central current density J_{tc}, the central q-value q_c, and the central beta β_c. Since there is no poloidal current, there is a one-to-one relation between these parameters. The regions of instability lie above the curves for J_{tc} and β_c and lie below the q_c curve.

The curves in Fig.19 include series of runs at b/a of 8,6,4,3,2,1. The m=1 curve cuts off at b/a=4 because at greater elongations the marginal point is buried so far under the m=3 curve that we have no confidence in our extrapolation to the marginal point. The m=3 mode is not continued below b/a=4 partly because we did not look for it in every series of runs and partly because its growth rate, its interval of instability, and its spatial extent are all so small for b/a≤2 that it is nearly impossible to excite.

It should be reemphasized that we are considering only fixed-boundary modes. The marginal points and growth rates for the plasma-vacuum free-boundary modes are known to be quite different from the fixed-boundary modes in the circular cylinder and elliptical cylinder cases studied before /7/, /9/, /18/.

It should also be kept in mind that all results presented here are based on a particular equilibrium (Eq.(25)). Preliminary studies of the m=1 mode on the uniform current rectangular equilibrium for $1 \leq b/a \leq 4$ and k•a = 1 indicated that the marginal current density does not increase with elongation, but may decrease.

In Figs.20 and 21 we confine our attention to the m=1 mode and we plot the marginal points for different values of k•a and b/a. The trends observed in the k•a=1 case persist as k•a is decreased to 1/2 and 1/3. It should be noted that the growth rates are substantially reduced as k•a is

decreased. Extrapolating to longer wavelengths, Figs.20 and 21 indicate that the marginal q-value goes to unity independent of b/a. Consequently the central current density J_{zc} scales like b/a, for large elongations, and like $1/\lambda$, for long wavelengths.

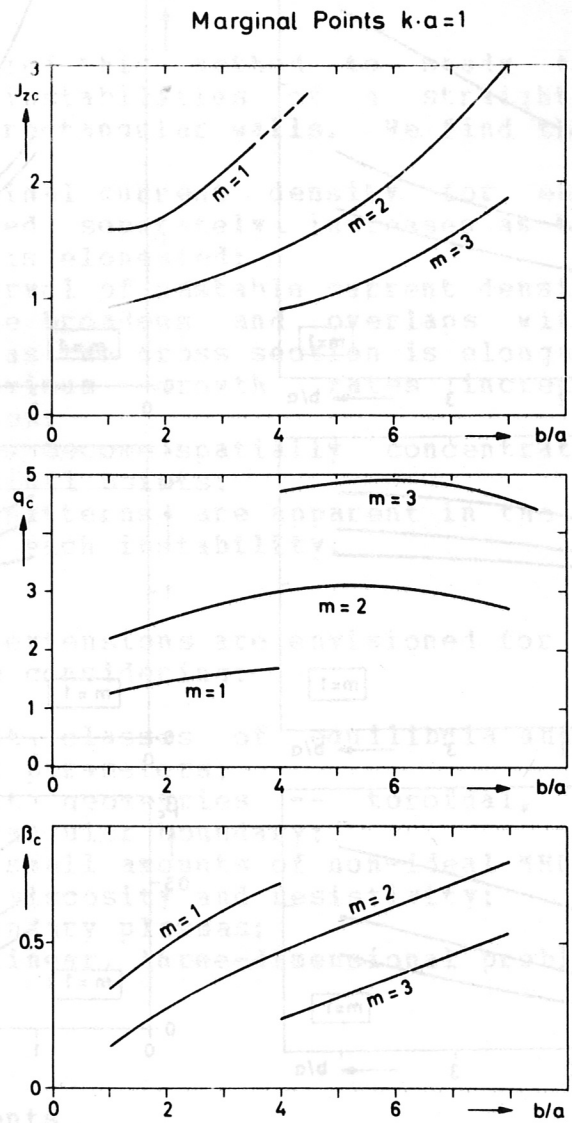

Fig. 19 Values of J_{zc}, q_c, and β_c at the low-current marginal points as a function of b/a for k·a=1 and m= 1,2,3.

By examining Figs.19, 20 and 21 we can answer the original question which motivated this investigation: can one force a higher current density through the plasma by elongating it? If we confine our interest to any one mode, the answer is yes. One gets dramatic improvements for the current density as b/a becomes greater than 2. The marginal β for each mode responds immediately as b/a is increased above 1. The marginal q -value for each mode reaches a

broad maximum as b/a is increased; this maximum shifts to higher b/a for higher m-modes.

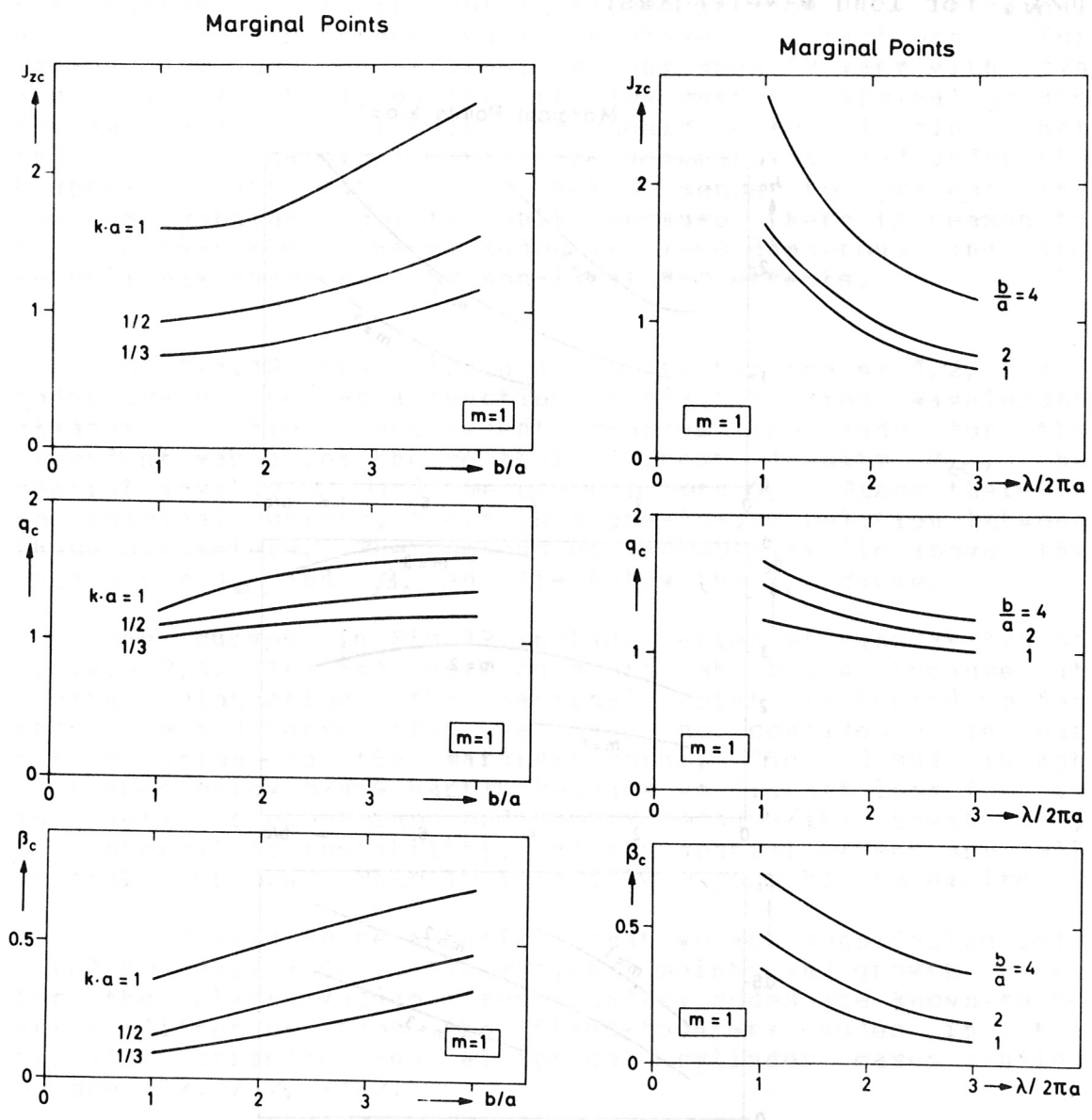

Figs. 20, 21 Marginal J_{zc}, q_c, and β_c for the m=1 mode as a function of b/a and $\lambda/2\pi a = (k \cdot a)^{-1}$.

However, if all the modes have equally important physical consequences, then Fig. 16 suggests that one cannot increase the current density (or β) by increasing the elongation. The higher m-modes become much more unstable with increasing b/a and their intervals of instability overlap with the lower m-modes.

5. Conclusions

We have demonstrated in this paper that gross MHD instabilities can be investigated by solving the linearized MHD equations as an initial boundary-value problem on the computer.

We have applied this method to study the ideal-MHD fixed-boundary instabilities of a straight cylindrical equilibrium with rectangular walls. We find that:

1) the marginal current density for each mode considered separately increases as the cross section is elongated;
2) the interval of unstable current densities for each mode broadens and overlaps with lower n-modes as the cross section is elongated;
3) the maximum growth rates increase with elongation;
4) the modes become spatially concentrated near the marginal points;
5) vortex patterns are apparent in the velocity field of each instability.

A number of extensions are envisioned for this method. Among them we are considering:

1) different classes of equilibria and a wider range of parameters;
2) different geometries -- toroidal, helical, non-rectangular boundary;
3) adding small amounts of non-ideal MHD effects such as viscosity and resistivity;
4) free-boundary plasmas;
5) the nonlinear, three-dimensional problem.

Acknowledgments

We are grateful to Dr. K.H. von Hagenow for the use of his equilibrium program and for many useful suggestions and fruitful discussions during the course of this work.

Many additional suggestions and encouragements were offered by the Garching Belt Pinch Group and by other members of the Experimental Division 1 and the Theory Division.

APPENDIX A

Initial Boundary-Value Problem:

The system of partial differential equations for the perturbed quantities $\vec{v}^1$, p^1 and $\vec{B}^1$ is written up in component form:

$$\rho^0 \frac{\partial}{\partial t} v_x^1 + \frac{\partial}{\partial x} p^1 - J_y^1 B_z^0 + J_z^1 B_y^0 - J_y^0 B_z^1 + J_z^0 B_y^1 = 0 \qquad (A1)$$

$$\rho^0 \frac{\partial}{\partial t} v_y^1 + \frac{\partial}{\partial y} p^1 - J_z^1 B_x^0 + J_x^1 B_z^0 - J_z^0 B_x^1 + J_x^0 B_z^1 = 0 \qquad (A2)$$

$$\rho^0 \frac{\partial}{\partial t} v_z^1 + ik\, p^1 - J_x^1 B_y^0 + J_y^1 B_x^0 - J_x^0 B_y^1 + J_y^0 B_x^1 = 0 \qquad (A3)$$

$$\frac{\partial}{\partial t} p^1 + v_x^1 \frac{\partial}{\partial x} p^0 + v_y^1 \frac{\partial}{\partial y} p^0 + \gamma p^0 \left(\frac{\partial}{\partial x} v_x^1 + \frac{\partial}{\partial y} v_y^1 + ik v_z^1\right) = 0 \qquad (A4)$$

$$\frac{\partial}{\partial t} B_x^1 + \frac{\partial}{\partial y} E_z^1 - ik\, E_y^1 = 0 \qquad (A5)$$

$$\frac{\partial}{\partial t} B_y^1 + ik\, E_x^1 - \frac{\partial}{\partial x} E_z^1 = 0 \qquad (A6)$$

$$\frac{\partial}{\partial t} B_z^1 + \frac{\partial}{\partial x} E_y^1 - \frac{\partial}{\partial y} E_x^1 = 0 \qquad (A7)$$

where $\vec{J}^1$ and $\vec{E}^1$ are defined by the following expressions:

$$J_x^1 = \frac{\partial}{\partial y} B_z^1 - ik\, B_y^1 \qquad (A8)$$

$$J_y^1 = ik\, B_x^1 - \frac{\partial}{\partial x} B_z^1 \qquad (A9)$$

$$J_z^1 = \frac{\partial}{\partial x} B_y^1 - \frac{\partial}{\partial y} B_x^1 \qquad (A10)$$

$$E_x^1 = - v_y^1 B_z^0 + v_z^1 B_y^0 \qquad (A11)$$

$$E_y^1 = - v_z^1 B_x^0 + v_x^1 B_z^0 \qquad (A12)$$

$$E_z^1 = - v_x^1 B_y^0 + v_y^1 B_x^0 \qquad (A13)$$

APPENDIX B

Energy Balance:

Multiplication of the basic equations with $\frac{1}{2}v^2$ (Eq. (1)), $\vec{v}$ (Eq. (2)), $1/(\gamma-1)$ (Eq. (3)), $\vec{B}$ (Eq. (4)) and adding them up yields the energy balance:

$$\frac{\partial}{\partial t}\left\{\frac{1}{2}\rho v^2 + \frac{1}{\gamma-1}p + \frac{1}{2}B^2\right\} + \nabla\left\{\left(\frac{1}{2}\rho v^2 + \frac{\gamma}{\gamma-1}p\right)\vec{v} + \vec{E}\times\vec{B}\right\} = 0$$

The energy balance of the linearized equations is derived either by linearizing this equation up to second order or adding up the linearized basic equations up to second order.

$$\frac{\partial}{\partial t}\left\{\frac{1}{2}\rho^0(\vec{v}^1)^2 + \frac{1}{\gamma-1}p^2 + \frac{1}{2}(\vec{B}^1)^2 + (\vec{B}^0\vec{B}^2)\right\} + \nabla\left\{\frac{\gamma}{\gamma-1}(p^1\vec{v}^1 + p^0\vec{v}^2) + \vec{E}^1\times\vec{B}^1 + \vec{E}^2\times\vec{B}^0\right\} = 0 \qquad (B1)$$

For the second order quantities $\vec{v}^2$, p^2, $\vec{B}^2$ the following equations can be derived:

$$\rho^0\frac{\partial}{\partial t}\vec{v}^2 + \rho^1\frac{\partial}{\partial t}\vec{v}^1 + \rho^0\vec{v}^1\nabla\vec{v}^1 + \nabla p^2 - \vec{J}^1\times\vec{B}^1 - \vec{J}^0\times\vec{B}^2 - \vec{J}^2\times\vec{B}^0 = 0 \qquad (B2)$$

$$\frac{\partial}{\partial t}p^2 + \nabla(p^1\vec{v}^1) + (\gamma-1)p^1(\nabla\vec{v}^1) + \nabla(p^0\vec{v}^2) + (\gamma-1)p^0(\nabla\vec{v}^2) = 0 \qquad (B3)$$

$$\frac{\partial}{\partial t}\vec{B}^2 + \nabla\times\vec{E}^2 = 0 \qquad (B4)$$

$$\vec{J}^2 = \nabla\times\vec{B}^2 \qquad (B5)$$

$$\vec{E}^2 + \vec{v}^1\times\vec{B}^1 + \vec{v}^2\times\vec{B}^0 = 0 \qquad (B6)$$

APPENDIX C

Difference Approximation:

An explicit method is used; i.e. the time derivative is approximated by

$$\frac{\partial}{\partial t} Y \longrightarrow \frac{Y_{i,k}(t+\Delta t) - Y_{i,k}(t)}{\Delta t}$$

$$\text{def.:} \quad \hat{Y}_{i,k} ::= Y_{i,k}(t+\Delta t)$$

all other terms are computed at the old timestep; hence:

$$\hat{Y}_{i,k} = f\left((Y_{l,m}),\ l=i-1,i,i+1;\ m=k-1,k,k+1 \right).$$

Space averages:

Note: the $Z_{i,k}$ quantities are defined half a mesh point ahead of the $Y_{i,k}$ quantities in both spatial directions. For the correct "centering" and averaging of the different quantities the following graph may be useful:

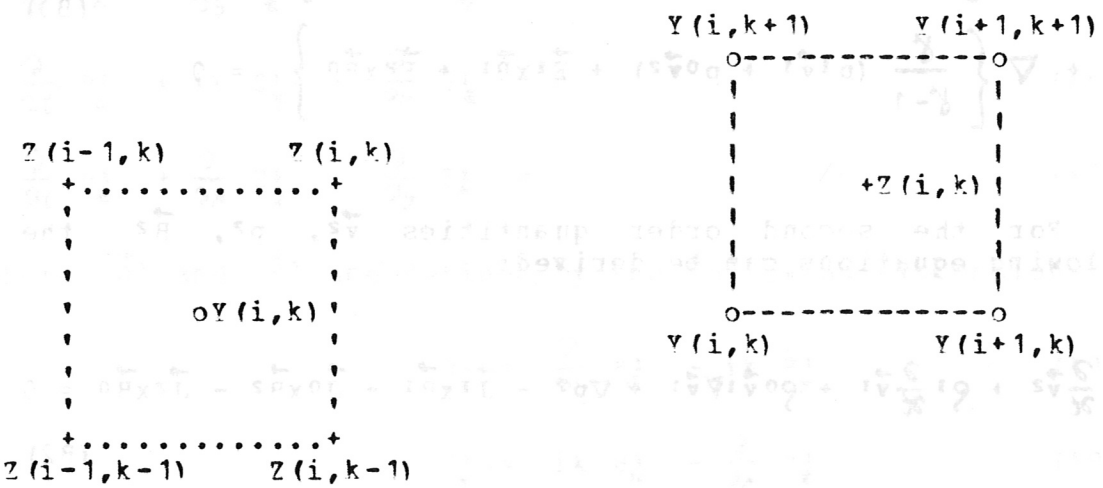

$$\langle Z_i \rangle_{k-1/2} ::= \frac{1}{2}\left(Z(i,k-1)+Z(i,k)\right)$$

$$\langle Z \rangle_{i-1/2,k-1/2} ::= \frac{1}{4}\left(Z(i-1,k-1)+Z(i,k-1)+Z(i-1,k)+Z(i,k)\right)$$

$$\langle Y_i \rangle_{k+1/2} ::= \frac{1}{2}\left(Y(i,k)+Y(i,k+1)\right)$$

$$\langle Y \rangle_{i+1/2,k+1/2} ::= \frac{1}{4}\left(Y(i,k)+Y(i+1,k)+Y(i,k+1)+Y(i+1,k+1)\right)$$

Example 1) x-component of the equation of motion (A1):

$$\rho^{\circ}_{i,k}\frac{\hat{v}^1_{i,k} - v^1_{i,k}}{\Delta t} + \frac{\langle p^1_i\rangle_{k-1/2} - \langle p^1_{i-1}\rangle_{k-1/2}}{\Delta x} + - J^1_{y\,i,k}\,B^0_{z\,i,k} +$$

$$+ J^1_{z\,i,k}\,B^0_{y\,i,k} - J^0_{y\,i,k}\langle B^1_z\rangle_{i-1/2,k-1/2} + J^0_{z\,i,k}\langle B^1_y\rangle_{i-1/2,k-1/2} = 0$$

Example 2) pressure equation (A4):

$$\frac{\hat{p}^1_{i,k} - p^1_{i,k}}{\Delta t} + \langle v^1_x\rangle_{i+1/2,k+1/2}\frac{\langle p^0_{i+1}\rangle_{k+1/2} - \langle p^0_i\rangle_{k+1/2}}{\Delta x} +$$

$$+ \langle v^1_y\rangle_{i+1/2,k+1/2}\frac{\langle p^0_{k+1}\rangle_{i+1/2} - \langle p^0_k\rangle_{i+1/2}}{\Delta v} +$$

$$+ \gamma\langle p^0\rangle_{i+1/2,k+1/2}\left\{\frac{\langle v^1_{x\,i+1}\rangle_{k+1/2} - \langle v^1_{x\,i}\rangle_{k+1/2}}{\Delta x} +\right.$$

$$+ \frac{\langle v^1_{y\,k+1}\rangle_{i+1/2} - \langle v^1_{y\,k}\rangle_{i+1/2}}{\Delta v} +$$

$$\left. + \quad ik\ \langle v^1_z\rangle_{i+1/2,k+1/2}\right\} = 0$$

Example 3) x-component of magnetic field equation (A5):

$$\frac{\hat{B}^1_{x\,i,k} - B^1_{x\,i,k}}{\Delta t} + \frac{\langle E^1_{z\,k+1}\rangle_{i+1/2} - \langle E^1_{z\,k}\rangle_{i+1/2}}{\Delta y} - ik\,\langle E^1_y\rangle_{i+1/2,k+1/2} = 0$$

APPENDIX D Equilibrium Properties

We have made our most intensive study of the equilibrium specified by

$$p'(\psi) = J_{zc}\psi/\psi_c, \quad \psi(\text{wall}) = 0$$
$$B_z^0 = 1 \quad , \rho^0 = 1 \tag{D1}$$

in a straight rectangular cylinder, for reasons described in section 4. A number of unexpected simplicities were found for this particular equilibrium: First an analytic solution exists:

$$\psi = \psi_c \sin\left(\frac{\pi x}{2a}\right) \cdot \sin\left(\frac{\pi y}{2b}\right) \tag{D2}$$

The origin here is at the lower left corner of the domain so that the maximum flux is in the center of the domain. Other possible solutions of Eq.(D1), with node lines running through the domain, will not be considered here. Using the equilibrium equation Eq.(21), the central flux ψ_c is related to the central current density J_{zc} by

$$\psi_c = J_{zc}/\left(\left(\frac{\pi}{2a}\right)^2 + \left(\frac{\pi}{2b}\right)^2\right) \tag{D3}$$

Then the pressure profile, from Eq.(D1), is:

$$p(\psi) = \frac{1}{2} J_{zc}\psi^2/\psi_c \tag{D4}$$

The poloidal B-field is determined from Eq.(20). The flux surfaces are illustrated in Fig.3.

As the rectangular boundary is elongated, the equilibrium has the interesting feature that all the nested flux surfaces have the same ratio of major to minor axes (vertical to horizontal dimensions). This statement holds true for any flux functions with the form $\psi(x,y) = f(x/a)\cdot f(y/b)$, where b/a is the ratio of the axes. If we examine any given flux surface, the ratio of the poloidal B-field at the midplane and at the vertical axis is also b/a. These features are identical to those of the elliptical equilibrium carrying uniform longitudinal current density.

But unlike the uniform current ellipse, the rotational transform for this equilibrium varies from a maximum value in the center to zero at the edge. The rotational transform t (the reciprocal of the q-value) is computed using the formula

$$1/t(\psi) = q = d\psi/d\chi \tag{D5}$$

using a program written by F.Pohl /20/ to compute the longitudinal flux $\chi(\psi)$ within a flux surface ψ = constant. The cross section of the rotational transform along the vertical axis is shown in Fig.22. The rotational transform goes to zero at the wall because the poloidal field has a stagnation point (is zero) in the corners.

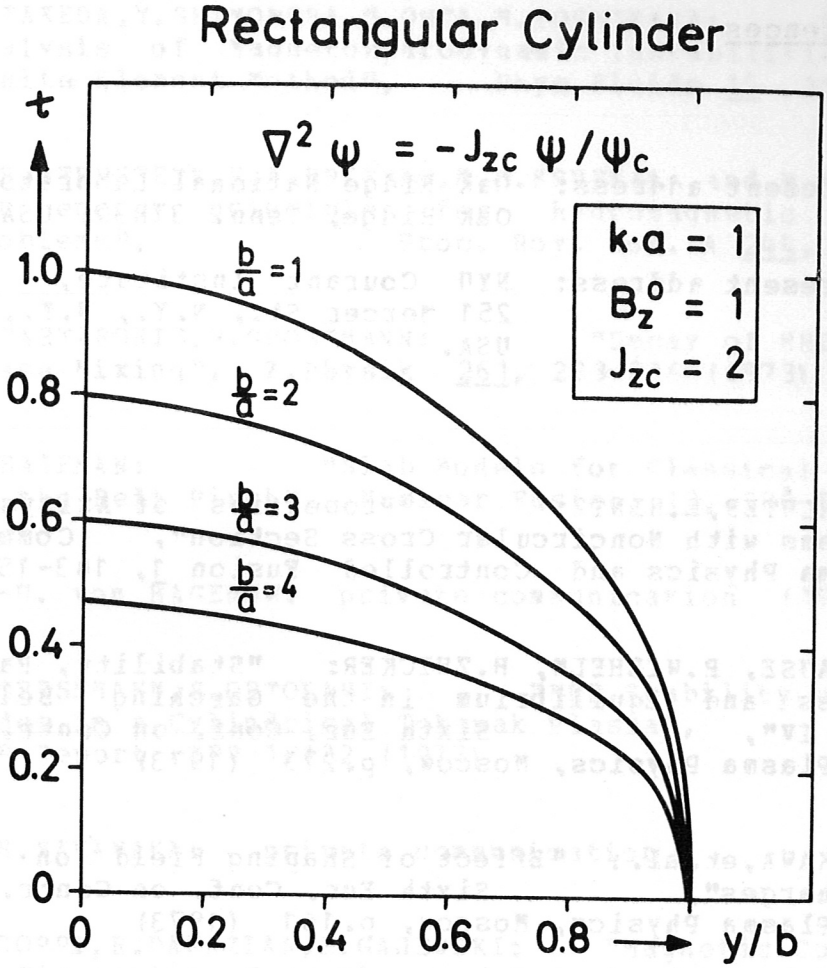

Fig.22 Rotational transform

The central q-value fits the empirical formula

$$q = \frac{k \cdot B_z^0}{J_{zc}} \cdot \frac{a^2 + b^2}{a \cdot b} \qquad (D6)$$

which is the same as the formula for the (uniform) q-value in the uniform current ellipse. The beta-value, defined locally by the formula

$$\beta \equiv \frac{p}{p + B^2/2} \qquad (D7)$$

can be calculated analytically. It assumes its maximum value in the center of the domain:

$$\beta_{max} = \frac{1}{1 + (B_z^0)^2\,(1/a^2 + 1/b^2)\,\pi^2/4J_{zc}^2} \qquad (D8)$$

References

+ Present address: Oak Ridge National Laboratory, Oak Ridge, Tenn. 37830, USA.

‡ Present address: NYU Courant Institute, 251 Mercer St., N.Y., N.Y., 10012, USA.

/ 1/ J.SCHLÜTER,E.HINTZ: "Properties of Axisysmmetric Systems with Noncircular Cross Section", Comments on Plasma Physics and Controlled Fusion 1, 143-153 (1972)

/ 2/ H.KRAUSE, R.WILHELM, H.ZWICKER: "Stability, Radiation Losses and Equilibrium in the Garching Belt Pinch ISAR IV", Sixth Eur. Conf. on Contr. Fusion and Plasma Physics, Moscow, p.273 (1973)

/ 3/ T.OHKAWA,et.al.: "Effect of Shaping Field on Doublet Discharges", Sixth Eur. Conf. on Contr. Fusion and Plasma Physics, Moscow, p.161 (1973)

/ 4/ K.-U. von HAGENOW, K.LACKNER: "On the Numerical Solution of MHD Equilibrium with Axisymmetry", Third International Symposium on Toroidal Plasma Confinement, Garching (1973)

/ 5/ W.FENEBERG, K.LACKNER: "Multipole Tokamak Equilibria", Nuclear Fusion 13, 549-557 (1973)

/ 6/ L.JANICKE: "Toroidal Equilibria of Plasmas with Beta=1 and strongly Noncircular Cross-section", Third International Symposium on Toroidal Plasma Confinement, Garching (1973)

/ 7/ V.D.SHAFRANOV: "Hydromagnetic Stability of a Current - carrying Pinch in a Strong Longitudinal Magnetic Field", Zh.Tekh.Fiz. 40 ,241 (1970) <Sov.Phys.Tech.Phys. 15 ,175 (1970)>

/ 8/ M.N.ROSENBLUTH,R.Y.DAGAZIAN,P.H.RUTHERFORD: "Nonlinear Properties of the Internal m = 1 Kink Instability in the Cylindrical Tokamak", Phys.Fluids 16, 1894 (1973)

/ 9/ T.TAKEDA,Y.SHIMOMURA,M.OHTA,M.YOSHIKAWA: "Numerical Analysis of Magnetohydrodynamic Instabilities by the Finite Element Method", Phys.Fluids 15 ,2193 (1972)

/10/ J.B.BERNSTEIN,E.A.FRIEMAN,M.D.KRUSKAL and R.M.KULSRUD: "An energy principle for hydromagnetic stability problems", Proc. Roy. Soc. A 244, 17 (1958)

/11/ J.TARTARONIS,W.GROSSMANN: "Decay of MHD Waves by Phase Mixing", Z.Physik 261, 203-216 (1973)

/12/ G.BATEMAN: "Slab Models for Classical Diffusion in the Belt Pinch", Nuclear Fusion, 13, 581-594 (1973)

/13/ K.-U. von HAGENOW: private communication (1973)

/14/ W.GROSSMANN,S.ORTOLANI: "MHD Stability of Helical Modes in a Cylindrical Tokamak Plasma", IPP Report IPP 1/132 (1973)

/15/ P.H.SAKANAKA: private communication

/16/ B.COPPI,R.DAGAZIAN,R.GAJEWSKI: "Magnetic Confinement Configuration for Plasmas Carrying High Currents", Phys.Fluids 15, 2405-2418 (1973)

/17/ J.P.FREIDBERG,F.A.HAAS,B.M.MARDER: "Kink Instabilities in High-Beta Tokamaks and Belt Pinches", Sixth Eur. Conf. on Contr. Fusion and Plasma Physics Moscow (1973) p. 87; and other reports to be published

/18/ G.LAVAL,R.PELLAT,J.L.SOULE: "Theoretical Results on MHD Stability of Tokamac Equilibria with Shaped Cross-Sections", Third International Symposium on Toroidal Plasma Confinement, Garching (1973), and other reports to be published.

/19/ D.LORTZ,J.NÜHRENBERG: "Comparison between Necessary and Sufficient Stability Criteria for Axially Symmetric Equilibria", Nuclear Fusion 13, 821-827 (1973)

/20/ F.POHL: private communication